

Steady low Reynolds number flow of a generalized Newtonian fluid through a slender elastic tube

Vishal Anand¹ and Ivan C. Christov^{1†}

¹School of Mechanical Engineering, Purdue University, West Lafayette, Indiana 47907, USA

(Received xx; revised xx; accepted xx)

Microfluidic devices are often manufactured using soft polymeric materials, while biological tissues are elastic. Consequently, both can deform significantly due to adjacent fluid flow, even at vanishing Reynolds number (no fluid inertia). Deformation leads to significant enhancement of flow due to the change in cross-sectional area that engenders a variable pressure gradient in the flow-wise direction; hence, a nonlinear flow rate–pressure drop relation (unlike the Hagen–Poiseuille law for a rigid tube). To capture non-Newtonian effects of biofluids, we employ the power-law rheological model. The structural problem is reduced to transverse loading of linearly-elastic cylindrical shells. A perturbative approach (in the slenderness parameter) yields analytical solutions for the flow and deformation. Specifically, using matched asymptotics, we obtain a uniformly valid solution, which features both a boundary layer and a corner layer, for the coupled flow–deformation problem in a thin, slender deformable microtube. Consequently, we obtain a “generalized Hagen–Poiseuille law” for soft microtubes. We benchmark the mathematical predictions against three-dimensional two-way coupled direct numerical simulations (DNS) of flow and deformation performed using the commercial computational engineering platform by ANSYS. The simulations establish the range of validity of the theory, showing excellent agreement for thin and slender soft microtubes.

Key words: Keywords will be added during the typesetting process

1. Introduction

Microfluidics is the study of the manipulation of microscopic volumes of fluids at small scales (Squires & Quake 2005). Though the subfield of fluid mechanics pertaining to flows at small scales, i.e., *low Reynolds number hydrodynamics* (Happel & Brenner 1983), is not a new field, its relevance to technologies at the microscale (and thus the emergence of the term “microfluidics”) occurred only in the 1990s (Bruus 2008). Technological advancements in microfabrication processes over the few past decades (Xia & Whitesides 1998; Kitson *et al.* 2012; Su *et al.* 2016), also reviewed in by Nguyen & Wereley (2006), have made microscale fluid mechanics more accessible experimentally. The insights gained thereby have been harnessed for a variety of applications, which in turn evinced keener interest in using microfluidics to solve global, medial and social problems (Whitesides 2006). The symbiotic relationship between basic science and human welfare thus sees one of its most vivid manifestations in the potential of microfluidics research. For example,

† Email address for correspondence: christov@purdue.edu; url: <http://tmnt-lab.org>

technological applications of microfluidics include electronic chip cooling (Weisberg *et al.* 1992; Dixit & Ghosh 2015), lab-on-a-chip devices (Abgrall & Gué 2007) such as lab-on-a-CD diagnostics (Madou *et al.* 2006; Kong *et al.* 2016), *in vitro* isolation of cancer cells (Nagrath *et al.* 2007) and clinical pathology (Sun *et al.* 2010), and various micro-total analysis (μ TAS) systems (Reyes *et al.* 2002; Auoux *et al.* 2002), amongst others. Microfluidic devices afford many advantages over their traditional counterparts: portability, low reagent consumption and short analyses times, often at higher resolutions than macroscopic counterparts (Nguyen & Wereley 2006).

A pernicious feature of microscale fluid mechanics is that fluid–structure interactions (FSIs) occur in both external and confined flows due to the compliance of the various solid-wall materials (Duprat & Stone 2016). For example, in inertialess locomotion (i.e., at low Reynolds number), a swimmer may be deformable (e.g., a bacterium has a flexible flagellum) or the fluid may be “deformable” (e.g., a polymeric substance dissolved into a liquid). On the one hand, in external flows, the elasticity of a swimmer affects its propulsive thrust and ability to navigate (Lauga 2016). On the other hand, in confined flows, the flow conduit may be made of a deformable material (Karan *et al.* 2018), such as polydimethylsiloxane (PDMS) (a polymeric gel) (Xia & Whitesides 1998) or elastin (a constituent of arteries) (Sandberg *et al.* 1977). Such “creeping” flows can delaminate an elastic membrane from a solid boundary, forming blisters (Chopin *et al.* 2008) that are prone to a wealth of mechanical instabilities (Juel *et al.* 2018) and whose inflation dynamics are sensitive to the contact line conditions (Hewitt *et al.* 2015). The hydrodynamic pressure within such conduits is affected by the deformation of the conduit as a result of two-way FSI. Specifically, the pressure drop across a soft microchannel is significantly smaller compared to the rigid case Gervais *et al.* (2006). Consequently, deviations are expected from the classical *Hagen–Poiseuille law* (Sutera & Skalak 1993), which relates the viscous pressure drop across a length of pipe to the the volumetric flow rate, fluid properties and physical dimensions. The goal of our study of *microscale fluid–structure interactions* is to mathematical analyze and quantify such deviations.

Extensive experimental work over the past decade has sought to address understand FSI in microfluidics, specifically the effect of FSI on the flow rate–pressure drop relationship in a soft microchannel (Gervais *et al.* 2006; Hardy *et al.* 2009; Seker *et al.* 2009; Ozsun *et al.* 2013; Kang *et al.* 2014; Raj *et al.* 2017). In one of the earliest works, Gervais *et al.* (2006) employed a scaling analysis to determine the relation between the maximal channel deformation and the hydrodynamic pressure within a soft PDMS-based microchannel. The top wall of the microchannel was allowed to be compliant, while the remaining three walls were held rigid. By inserting the scaling relationship into the *Hagen–Poiseuille law* for a rectangular microchannel, Gervais *et al.* (2006) captured the observed nonlinear (quartic) relationship between the flow rate and the pressure drop for a Newtonian fluid (water). However, the approach of Gervais *et al.* (2006) is not predictive because it contains a fitting parameter (the unknown proportionality constant in the scaling relationship), which has to be determined *a posteriori* by experiments.

Christov *et al.* (2018) analyzed the problem of steady FSI in a microchannel via perturbation methods. Specifically, they determined the flow rate–pressure drop relation for a long, shallow microchannel with a compliant top wall by coupling a Kirchhoff–Love thin-plate theory to viscous flow under the lubrication approximation. Confirming the observation of Gervais *et al.* (2006), it was shown by Christov *et al.* (2018) that the flow rate–pressure drop relation is a quartic polynomial and the fitting parameter was thus eliminated through mathematical analysis. This approach was extended to capture thick top walls, via the first-order shear deformation plate theory of Mindlin (1951), and extensively validated computationally by Shidhore & Christov (2018) via

fully-3D two-way coupled direct numerical simulations. More importantly, however, in (Christov *et al.* 2018; Shidhore & Christov 2018) the cross-sectional deformation profile of the microchannel's compliant wall was determined. The perturbation approach's generality is appealing as, in theory, higher-order corrections to the flow rate–pressure drop relation can be obtained along the lines of Tavakol *et al.* (2017), who developed an *extended* lubrication theory. This approach is valid for channels with modest aspect ratios and with shape changes on the order of the channel height.

The study of moderate-Reynolds-number instabilities due to FSIs in soft tubes is a time-honored subject (Grotberg 1994; Grotberg & Jensen 2004; Heil & Hazel 2011) primarily due to their relevance in modeling biological flow in the arteries and the lungs. Consequently, microtubes traditionally reside on the opposite end of the FSI spectrum from microchannels, in terms of Reynolds number. Specifically, the study of *collapsible tubes* interrogates the case of microtubes whose radius *decreases* owing to negative transmural pressure difference and eventually can completely collapse (Shapiro 1977; Bertram & Pedley 1982). Here, the flow field is one-dimensional, averaged across the cross section, but not developed (Shapiro 1977). Viscous effects are captured using a pipe flow friction factor. A *tube law* is obtained to relate the local transmural pressure difference to the change in area due to circumferential and axial bending and tension, from postulated simple relations (Shapiro 1977) to rigorous derivations from shell theory (Whittaker *et al.* 2010). Even though the problem of collapsible tubes involves liquid flow, Shapiro (1977) elegantly explained the analogy to gas dynamics: a *speed index*, akin to the Mach number, divides the flow into subcritical and supercritical regimes. The relevance of this moderate-to-high-Reynolds number FSI in soft tubes is evident in biofluid mechanics (Pedley 1980; Kizilova *et al.* 2012), for example in the contraction of the trachea during bouts of coughs (Grotberg 1994). The mathematical analysis of stability of such flows in three-dimensions is an ongoing challenge (Gay-Balmaz *et al.* 2018). Nevertheless, there is also a need to develop accurate models for low-Reynolds-Number FSI in soft tubes due to the relevance to blood flow through small arteries (Čanić & Mikelić 2003).

Most the latter research has focused on Newtonian fluids. Biofluids are, however, non-Newtonian (Chakraborty 2005; Lee 2006) with blood being often modeled a Casson fluid, which has both a yield stress and a shear-dependent viscosity (Fung 1993, Ch. 3). Research on microscale FSIs has only just begun to take into account the non-Newtonian nature of the working fluids (Raj & Sen 2016; Boyko *et al.* 2017; Raj M *et al.* 2018; Anand *et al.* 2018). With further relevance to biofluid mechanics, Raj M *et al.* (2018) performed experiments on FSIs in a microchannel with *circular* cross-section, which is more akin to a microtube, or a blood vessel. The microchannel was fabricated using a pull-out soft lithography process out of PDMS. A non-Newtonian blood-analog fluid (xanthan gum) was pumped through the microchannel. Measurements of the pressure drop at different inlet flow rates was shown to match a simple mathematical model of one-way FSI, meaning that the pressure was calculated using the Hagen–Poiseuille law for a rigid tube and then imposed as a load on the structure, without coupling the microchannel shape change back into the hydrodynamic pressure.

In a recent series of works (Elbaz & Gat 2014, 2016; Boyko *et al.* 2017), two-way coupling was captured through a mathematical analysis of the transient pressure and deformation characteristics of a shallow, deformable microtube. Employing the Love–Kirchhoff hypothesis, a relation was obtained between the internal pressure load in a soft tube and its radial and axial deformation, up to the leading order in slenderness. Treating the structural problem as quasi-static, an unsteady diffusion-like equation for the fluid pressure was obtained and analyzed for both Newtonian (Elbaz & Gat 2014, 2016) and non-Newtonian (Boyko *et al.* 2017) fluids. However, the case of the steady flow

or the resulting flow rate–pressure drop relation for the microtube was not considered or benchmarked against simulations and/or experiments. Anand *et al.* (2018) achieved the latter for non-Newtonian microchannel FSI, leaving the mircotube case an open problem.

Finally, elastic deformation of structure need not always be a peripheral, unwanted effect in microscale flows. FSIs can also be employed for passive control of flows in microchannels (Leslie *et al.* 2009; Holmes *et al.* 2013; Gomez *et al.* 2017). For example, Holmes *et al.* (2013) carried out an experimental investigation of mechanically-actuated flow control within a flexible microchannel through a series of arches placed in the microchannel that function as valves to regulate and direct the flow. Meanwhile, Gomez *et al.* (2017) harnessed an elastic snap–through mechanism to design a microfluidic fuse. In a microchannel with a thin elastic strip as one wall, buckling of the arch by the viscous flow underneath allows passive rapid transition between a constricted and an unconstricted flow state (with concomitant rapid changes in the flow conductivity of the microchannel).

Thus, it should be clear that microscale FSIs are an important problem in mechanics. More importantly, however, recent results in the literature (e.g., Elbaz & Gat 2014; Boyko *et al.* 2017; Christov *et al.* 2018) suggest that asymptotic and perturbation methods can capture these fluid–structure interactions. To this end, in this paper, we present a comprehensive theoretical and computational study of steady FSIs in deformable microtubes. Since biofluids are, in general, non-Newtonian, we consider not just Newtonian fluids but also a generalized Newtonian fluid with a power-law shear-dependent viscosity, which is a suitable rheological model for steady flows. To capture the compliance of the (initially) cylindrical flow conduit, we employ classical (linear) shell theories. In §2, we describe the problem of interest with detailed specifications pertaining to the physical domain, the flow and the deformation. Then, in §3, we solve for the flow field under the lubrication approximation. Similarly, in §4, we employ thin-shell theories to solve for the deformation field. We bring all this together in §5, where the flow and the deformation fields are coupled, yielding a complete theory of linear FSI between a non-Newtonian fluid and a microtube. In §6, prediction from the theory developed in this paper are benchmarked against full two-way coupled and three-dimensional direct numerical simulations (DNS) of steady-state FSI carried out using commercial computational engineering tools. The benchmark against DNS, allows us to both validate our mathematical results as well as to determine the theory’s range of applicability. Finally, §7 summarizes our results and presents an outlook for future work.

2. Preliminaries

We consider an initially cylindrical flow conduit geometry as shown in Fig. 1. The geometry is assumed to be *slender*, i.e., its stream-wise dimension is much larger than its cross-sectional dimension, and *shallow* (or, *thin*), i.e., its thickness is much smaller than its cross-sectional dimension. The cylindrical coordinate system has its origin at the center of the inlet of the tube but it is displaced in Fig. 1 for clarity. The wall of the microtube has a finite thickness and it is soft; hence, it deforms due to the fluid flow within it. Specifically, the microtube has an undeformed radius a , a constant length ℓ , and constant (within the classical shell theories to be discussed below) thickness t . The radial deformation of the microtube is denoted by $u_r(z)$ so that the radius of the deformed tube is $R(z) = a + u_r(z)$. Axisymmetry ensures the latter only depend on the flow-wise coordinate z . The microtube’s wall is composed of a linearly elastic material with constant modulus of elasticity (Young’s modulus) E and a constant Poisson ratio ν .

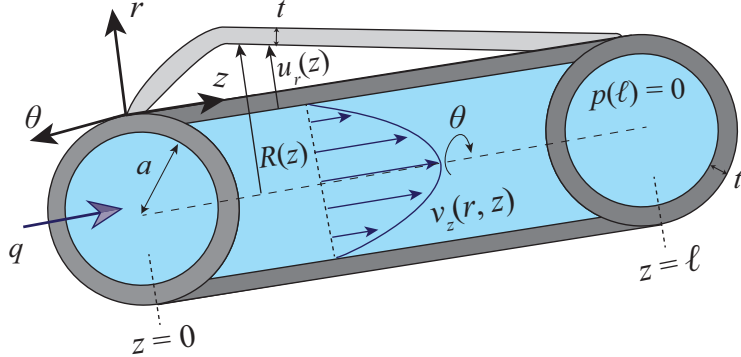


Figure 1: Schematic of the microtube geometry, labeling the variables, in its initial configuration. The notation for deformation is also labeled, although, for clarity, the deformation is not shown as being axisymmetric.

Fully-developed steady flow of a non-Newtonian fluid enters the microtube across the inlet ($z = 0$ plane) at a constant flow rate q . The non-Newtonian behavior of the fluid is due to its shear-dependent viscosity. Our main objective is to determine the relation between the pressure drop Δp , across the length of the microtube, and the imposed flow rate q . In other words, we seek to derive, mathematically, the Hagen–Poiseuille law for steady non-Newtonian flow in a deformable tube. To this end, we simplify the fluid flow (§3) and structural mechanics (§4) problems independently in the appropriate asymptotic limit(s). Then, we solve the two sets of governing equations, which are coupled together by the hydrodynamic pressure (the normal forces exerted by the fluid), which act as a load on the structure.

3. Fluid mechanics problem

The following assumptions pertaining to the fluid flow problem are made:

- (i) Steady flow: $\partial(\cdot)/\partial t = 0$.
- (ii) Axisymmetric flow: $\partial(\cdot)/\partial\theta = 0$ and $v_\theta = 0$.
- (iii) Slender tube: $\ell \gg a \Leftrightarrow \epsilon := a/\ell \ll 1$.

Assumption (iii) is key to our analysis. Davis (2017) highlights the “importance of being thin” in making analytical progress on nonlinear fluid mechanics problems.

First, we determine the kinematics of the flow. In the cylindrical coordinates labeled in Fig. 1, and under assumption (ii) above, the fluid’s equation of continuity (conservation of mass) is

$$\frac{1}{r} \frac{\partial}{\partial r} (r v_r) + \frac{\partial v_z}{\partial z} = 0. \quad (3.1)$$

Let us now introduce the following dimensionless variables:

$$\bar{r} = r/a, \quad \bar{p} = p/\mathcal{P}_c, \quad \bar{z} = z/\ell, \quad \bar{v}_z = v_z/\mathcal{V}_z, \quad \bar{v}_r = v_r/\mathcal{V}_r, \quad (3.2a, b, c, d, e)$$

Here, \mathcal{V}_z and \mathcal{V}_r are characteristic velocity scales in the axial and radial directions respectively, while \mathcal{P}_c is the characteristic pressure scale: e.g., the full pressure drop in pressure-controlled scenarios or the viscous pressure scale in flow-rate-controlled situations, which can be determined from the velocity scale [see Eq. (3.11) below].

Introducing the dimensionless variables from Eq. (5.33), Eq. (3.1) becomes

$$\frac{1}{\bar{r}} \frac{\partial}{\partial \bar{r}} (\bar{r} \bar{v}_{\bar{r}}) \frac{\mathcal{V}_r}{a} + \frac{\partial \bar{v}_{\bar{z}}}{\partial \bar{z}} \frac{\mathcal{V}_z}{\ell} = 0. \quad (3.3)$$

Balancing all terms in Eq. (3.3) yields the characteristic radial velocity scale: $\mathcal{V}_r \equiv \epsilon \mathcal{V}_z$. Consequently, to the leading order in ϵ , the velocity field is *unidirectional* (Leal 2007): $\bar{v} = \bar{v}_{\bar{z}}(\bar{r}) \hat{\mathbf{k}}$, where $\hat{\mathbf{k}}$ is the unit normal vector in the z -direction. Below, we show that, due to FSI, the unidirectional profile “picks up” a weak \bar{z} dependence as well, which is “allowed” under the *lubrication approximation* (Leal 2007; Bruus 2008).

Next, we consider the dynamics of the flow field. Since we are dealing with flow at the microscale, the Reynolds number Re (to be properly defined below upon introducing the fluid’s rheology) is assumed to be small (i.e., $Re \ll 1$), and the lubrication approximation applies. Consequently, inertial forces in fluid are negligible in comparison to pressure and viscous forces, and we begin our analysis with the following simplified equations expressing the momentum conservation in the (radial) r - and (axial) z -directions (Bird *et al.* 1987):

$$0 = \frac{1}{r} \frac{\partial}{\partial r} (r \tau_{rr}) + \frac{\partial \tau_{zr}}{\partial z} - \frac{\tau_{\theta\theta}}{r} - \frac{\partial p}{\partial r}, \quad (3.4a)$$

$$0 = \frac{1}{r} \frac{\partial}{\partial r} (r \tau_{rz}) + \frac{\partial \tau_{zz}}{\partial z} - \frac{\partial p}{\partial z}. \quad (3.4b)$$

Here, τ is the fluid’s shear stress tensor, and p is the hydrodynamic pressure. We have already made use of the assumptions of axisymmetry in Eqs. (3.4). The same assumption also leads to the momentum equation in θ direction being reduced to zero *identically*.

Now, we need to express the rate-of-strain tensor $\dot{\gamma}$ in terms of the velocity components. It is wise to use all the results (axisymmetric unidirectional flow with only a z -component) so far to simplify this calculation. Then, for the chosen cylindrical coordinate system, the only non-vanishing rate-of-strain components (in terms of the velocity gradient) are

$$\dot{\gamma}_{zz} = 2 \frac{\partial v_z}{\partial z}, \quad (3.5a)$$

$$\dot{\gamma}_{rz} = \dot{\gamma}_{zr} = \frac{\partial v_r}{\partial z} + \frac{\partial v_z}{\partial r} = \frac{\partial v_z}{\partial r}. \quad (3.5b)$$

We use the dimensionless variables from Eq. (5.33) to rewrite Eqs. (3.5) as

$$\dot{\gamma}_{zz} = \frac{2\epsilon \mathcal{V}_z}{a} \frac{\partial \bar{v}_{\bar{z}}}{\partial \bar{z}}, \quad (3.6a)$$

$$\dot{\gamma}_{rz} = \dot{\gamma}_{zr} = \frac{\mathcal{V}_z}{a} \frac{\partial \bar{v}_{\bar{z}}}{\partial \bar{r}}. \quad (3.6b)$$

Clearly, $\dot{\gamma}_{zz} = \mathcal{O}(\epsilon)$, while $\dot{\gamma}_{rz}, \dot{\gamma}_{zr} = \mathcal{O}(1)$. Therefore, to a leading order in ϵ , the rate-of-strain tensor has a single component, consistent with the kinematic reduction to unidirectional flow. Consequently, the only non-zero component of the shear stress tensor is τ_{rz} .

Taking into account the above deliberations, the momentum conservation equations (3.4) become

$$0 = \frac{\partial p}{\partial r}, \quad (3.7a)$$

$$0 = \frac{1}{r} \frac{\partial}{\partial r} (r \tau_{rz}) - \frac{\partial p}{\partial z}. \quad (3.7b)$$

Equation (3.7a) implies that the pressure is at most a function of z , i.e., $p = p(z)$. This

result is as far as we can go at this stage. Next, we need to specify the constitutive equation relating τ to $\dot{\gamma}$ to connect the *kinematics* of the flow problem to its *dynamics*.

Keeping biofluid mechanics applications in mind, we consider the fluid to be non-Newtonian fluid. Blood is known to exhibit shear-dependent viscosity at steady state, and it is often modeled as a *Casson fluid*, which captures both a yield stress and a shear-dependent viscosity (Fung 1993, Ch. 3). However, detecting the yield stress (at zero shear rate) in a suspension of blood cells is extremely difficult (perhaps even “controversial” as discussed by Balmforth *et al.* (2014)), and some experiments (Chien *et al.* 1966) show it to be vanishing (see also Fung 1993, p. 65). Therefore, we consider the special case of zero yield stress, which reduces the Casson fluid model to the *power-law fluid* (also known as Ostwald–de Waele (Bird 1976)) model. Then, utilizing Eq. (3.5b), the shear stress is expressed in terms of rate of strain as

$$\tau_{rz} = \eta \dot{\gamma}_{rz} = \eta \frac{\partial v_z}{\partial r}, \quad \eta = m \left| \frac{\partial v_z}{\partial r} \right|^{n-1}, \quad (3.8a, b)$$

where η is the *apparent viscosity*, m is the *consistency factor* (a non-negative real number), and n is the *power-law index* (also a non-negative real number). Now, the appropriate definition of the Reynolds number given the above non-dimensionalization and power-law rheology is $Re = \varrho a^n \mathcal{V}_z^{2-n} / m$ (see also Crespí-Llorens *et al.* 2015), where ϱ is the fluid’s density. As usual, $n < 1$ corresponds to shear-thinning fluids, such as blood (Chien *et al.* 1966), in which the apparent viscosity decreases with shear rate. On the other hand, $n > 1$ corresponds to shear-thickening fluids in which the apparent viscosity increases with shear rate, giving rise to applications for ballistic armor, such as woven Kevlar fabrics impregnated with a colloidal suspension of silica particles (Wagner & Brady 2009). Although the most common biofluid, namely blood, is shear-thinning or pseudoplastic ($n < 1$), our analysis nevertheless captures Newtonian ($n = 1$, in which case $m = \mu$, i.e., the shear viscosity) and shear-thickening or dilantant ($n > 1$) behavior as well through the rheological model in Eq. (3.8).

For axisymmetric flow, we expect that the axial velocity will attain its maximum along the centerline ($r = 0$), decreasing with the radius until it reaches zero at the tube wall (due to no slip) in this steady flow. Consequently, the velocity gradient is negative and $|\partial v_z / \partial r| = -\partial v_z / \partial r$. Then, in terms of the dimensionless variables, Eq. (3.8) becomes

$$\tau_{rz} = -m \left(\frac{\mathcal{V}_z}{a} \right)^n \left(-\frac{\partial \bar{v}_z}{\partial \bar{r}} \right)^n. \quad (3.9)$$

Substituting the latter expression for τ_{rz} along with the dimensionless pressure into the z -momentum equation (3.7b) yields

$$\frac{1}{\bar{r}} \frac{\partial}{\partial \bar{r}} \left[\bar{r} \left(-\frac{\partial \bar{v}_z}{\partial \bar{r}} \right)^n \right] = - \left(\frac{\mathcal{P}_c a^{n+1}}{\ell \mathcal{V}_z^n m} \right) \frac{d\bar{p}}{d\bar{z}}. \quad (3.10)$$

This equation sets the relationship between the pressure and velocity scales. Since the terms on the left- and right-hand side of Eq. (3.10) must be both $\mathcal{O}(1)$, we deduce that the term in parentheses on the right hand side of the equation should be

$$\left(\frac{\mathcal{P}_c a^{n+1}}{\ell \mathcal{V}_z^n m} \right) \equiv 1 \quad \Leftrightarrow \quad \mathcal{V}_z = \left(\frac{a^{n+1} \mathcal{P}_c}{m L} \right)^{1/n}. \quad (3.11a, b)$$

This equation relates the velocity and pressure scales. In a flow-rate-controlled experiment/simulation, we can choose a velocity scale $\mathcal{V}_z = q/(\pi a^2)$ based on the inlet flow rate q , and then the pressure scale \mathcal{P}_c can be calculated from Eq. (3.11). Thus, Eq. (3.10)

becomes

$$\frac{\partial}{\partial \bar{r}} \left[\bar{r} \left(-\frac{\partial \bar{v}_z}{\partial \bar{r}} \right)^n \right] = -\frac{d\bar{p}}{d\bar{z}} \bar{r}. \quad (3.12)$$

Integrating this equation with respect to \bar{r} and requiring that \bar{v}_z to be finite along the centerline as well as enforcing no slip, $\bar{v}_z(\bar{r} = \bar{R}) = 0$, yields

$$\bar{v}_z = \left(-\frac{1}{2} \frac{d\bar{p}}{d\bar{z}} \right)^{1/n} \left(\frac{\bar{R}^{1+1/n} - \bar{r}^{1+1/n}}{1 + 1/n} \right), \quad (3.13)$$

where $\bar{R} = R/a$ is the dimensionless deformed microtube radius. Note that \bar{R} is not necessarily unity because we allow the microtube to deform due to FSI, as discussed in the next section. As a result, while \bar{p} is at most a function of \bar{z} , \bar{v}_z can depend upon both \bar{r} and \bar{z} .

4. Structural mechanics problem

In §3, the set of three-dimensional momentum conservation equations for a power-law fluid were reduced to unidirectional flow, explicitly dependent only on the radial coordinate, up to the leading order. This reduction was achieved by prudently harnessing the assumptions of axisymmetry and slenderness, along with the lubrication approximation.

In a similar manner, we now proceed to tackle the structural mechanics problem of the tube's deformation. The equations stating the equilibrium of forces in this problem are again three dimensional. To reduce the dimensionality of the problem, and make it tractable analytically, we employ some simplifying assumptions (itemized next), along with classical shell theories, which are two-dimensional approximations to three-dimensional displacement fields. Pertaining to the structural aspect of the problem, we have the following assumptions:

- (i) The cylinder is thin; its thickness is negligible compared to its radius: $t \ll a$.
- (ii) The cylinder is slender; its radius is small compared to its length: $a \ll \ell$.
- (iii) The material of the tube is isotropic and linearly elastic, with elasticity (Young's) modulus E and Poisson ratio ν .
- (iv) The strains are small, so the relationship between strain and displacement is linear.

Here, assumptions (iii) and (iv) ensure that the relation between stress and displacement is linear and thus the corresponding theory developed in this paper pertains to what we shall term *linear* FSI. The ramifications of assumptions (i) and (ii) will be discussed below.

A shell is materialization of a surface and, hence, is a three-dimensional entity by definition (Flügge 1960). A shell *theory* attempts to capture the dynamics of a shell in two dimensions and is thus *de jure* an approximate theory. Approximations are introduced in every facet of shell theory, namely the strain–displacement relation (*kinematics*), the stress equilibrium relation (*dynamics*), and the stress–strain relation (*constitutive*). There are many shell theories, of varying degree of approximation, and the treatment here cannot be exhaustive. For further details, the reader is directed to the classic monographs by Kraus (1967), Flügge (1960), and Timoshenko & Woinowsky-Krieger (1959). We focus only on the “simplest” shell theories capable of describing the FSI problem being posed.

4.1. Membrane theory

Owing to the thinness assumption ($t \ll a$), the microtube can be analyzed using membrane theory (sometimes referred to as “pressure vessel” theory) for sufficiently small a/t . Membrane theory of shells pertains to structures that sustain only tensions,

in the axial and circumferential directions, but cannot support bending or twisting moments (Flügge 1960, Ch. 3).† Membrane theory allows us to write the axial σ_{zz} and circumferential $\sigma_{\theta\theta}$ stresses (and the corresponding stress resultants) directly using only the equilibrium equations and the boundary conditions (see, e.g., Flügge 1960; Dym 1990):

$$\sigma_{\theta\theta} = p(z)a/t, \quad (4.1a)$$

$$\sigma_{zz} = p(z)a/(2t). \quad (4.1b)$$

Here, the hydrodynamic pressure $p(z)$ provides the load, and we have shown above that p is, at most, a function of z . Therefore, the normal stress resultant in the axial direction is simply

$$N_z = p(z)a/2. \quad (4.2)$$

Using the constitutive equations for linear elasticity, we obtain the circumferential strain as:

$$\epsilon_{\theta\theta} = \frac{1}{E}(\sigma_{\theta\theta} - \nu\sigma_{zz}) = (1 - \nu/2)\frac{a}{Et}p(z). \quad (4.3)$$

This yields the radial deformation profile along the microtube:

$$u_r(z) = a\epsilon_{\theta\theta} = (1 - \nu/2)\frac{a^2}{Et}p(z). \quad (4.4)$$

Under the membrane theory, displacement is simply proportional pressure, with the geometric and elasticity parameters setting the proportionality constant.

4.2. Donnell shell theory

Out of several shell theories based on the Love–Kirchhoff hypothesis (Love 1944), postulated for thin shells of revolution, perhaps the earliest and the most popular is Donnell's shell theory (Donnell 1933). It has been shown elsewhere that Donnell's shell theory is a straightforward extension of the thin plate theory to shells (Kraus 1967), which itself is an extension of the Euler-beam hypothesis to two dimensions. Furthermore, for the special case of axisymmetric loads with zero curvature, Donnell's shell theory reduces identically to the Love–Kirchhoff thin-plate theory (Kraus 1967), which we have successfully employed to analyze microchannel FSIs (Christov *et al.* 2018; Anand *et al.* 2018). Improving upon the membrane theory of §4.1, Donnell's shell theory takes into account the effect of bending and twisting moments (Kraus 1967).

According to Donnell's shell theory, the normal stress resultant N_z is related to the displacements u_r and u_z as

$$N_z = \frac{D}{a} \left(a \frac{du_z}{dz} + \nu u_r \right), \quad (4.5)$$

where $D = Et/(1 - \nu^2)$ is the *extensional rigidity* of the shell. Using Eqs. (4.2) and (4.5), we can eliminate N_z and obtain an ordinary differential equation (ODE) in the displacements:

$$\frac{p(z)a}{2} = \frac{D}{a} \left(a \frac{du_z}{dz} + \nu u_r \right). \quad (4.6)$$

Similarly, the equation governing the momentum balance in the radial direction is found

† This membrane theory is to be contrasted to, e.g., the highly nonlinear Föppl–von Kármán theory (Timoshenko & Woinowsky-Krieger 1959) of topologically rectangular thin plates (also often termed membranes).

to be (Dym 1990, Ch. 4):

$$\nu a \frac{du_z}{dz} + u_r + \frac{Ka^2}{D} \frac{d^4 u_r}{dz^4} = \frac{p(z)a^2}{D}, \quad (4.7)$$

where $K = Et^3/[12(1 - \nu^2)]$ is the *bending (flexural) rigidity* of the shell. We eliminate the axial displacement u_z from Eqs. (4.6) and (4.7) and substitute the expressions for D and K to obtain an ODE for the radial deflection $u_r(z)$ forced by hydrodynamic pressure $p(z)$:

$$\frac{Et^3}{12(1 - \nu^2)} \left[\frac{d^4 u_r}{dz^4} + \frac{12(1 - \nu^2)}{a^2 t^2} u_r \right] = (1 - \nu/2)p(z). \quad (4.8)$$

To understand the dominant balance(s) in Eq. (4.8), we introduce dimensionless variables, some of which are restated from Eq. (5.33), as follows:

$$\bar{z} = z/\ell, \quad \bar{u}_r = u_r/\mathcal{U}_c, \quad \bar{p} = p/\mathcal{P}_c, \quad (4.9a, b, c)$$

where, as before, \mathcal{P}_c is the characteristic pressure scale. The characteristic scale for the radial deflection of the tube, \mathcal{U}_c , is to be determined self-consistently as part of this analysis. Substituting the dimensionless variables from Eq. (4.9) into Eq. (4.8) yields

$$\left(\frac{t}{a} \right)^2 \left(\frac{a}{\ell} \right)^4 \frac{d^4 \bar{u}_r}{d\bar{z}^4} + 12(1 - \nu^2) \bar{u}_r = \frac{12(1 - \nu^2)a^2 \mathcal{P}_c}{Et \mathcal{U}_c} (1 - \nu/2) \bar{p}. \quad (4.10)$$

For a thin and slender shell we can neglect, in an order of magnitude sense to the leading order in t/a and a/ℓ , the first term on the left-hand side of Eq. (4.10) to obtain:

$$\bar{u}_r = \frac{a^2 \mathcal{P}_c}{Et \mathcal{U}_c} (1 - \nu/2) \bar{p}. \quad (4.11)$$

Since Eq. (4.11) represents a leading-order balance, comparing coefficients on both sides of the equation yields the deformation scale

$$\mathcal{U}_c = \frac{a^2 \mathcal{P}_c}{Et}. \quad (4.12)$$

Hence, the deformed tube radius is

$$\bar{R}(\bar{z}) \equiv \frac{a + u_r(z)}{a} = 1 + \beta \bar{u}_r(\bar{z}), \quad (4.13)$$

where $\beta := \mathcal{U}_c/a$ is a dimensionless parameter that controls the fluid-structure interaction. It is a measure of how large the structural deflection \mathcal{U}_c is compared to the undeformed radius a . A larger value of β corresponds to “stronger” fluid-structure coupling and, thus, a larger deflection.

Thus, at the leading order in t/a and a/ℓ , the dimensionless radial deflection is simply

$$\bar{u}_r(\bar{z}) = (1 - \nu/2) \bar{p}(\bar{z}). \quad (4.14)$$

Note that, Eq. (4.14) is identically the dimensionless version of our membrane theory result Eq. (4.4).

REMARK 1. *Sanders’ first approximation for thin shells preserves all the assumptions of the Love-Kirchhoff hypothesis but avoids inconsistencies arising in rigid-body motion (Kraus 1967; Sanders Jr. 1959). For axisymmetrically loaded shells of revolution, such as the ones treated herein, the governing equation of Sanders is the same as that of Donnell (Kraus 1967), i.e., Eq. (4.8). Hence, the analysis above carries through in the same way.*

REMARK 2. To the leading order in t/a and a/ℓ , the shell theory considered here yields the same equation as membrane theory, namely Eq. (4.4), which dictates that the radial deflection of the tube is directly proportional to the pressure at a given flow-wise cross-section. This observation is in agreement with the results in (Elbaz & Gat 2014, 2016), taking into account, of course, the different boundary conditions employed therein.

REMARK 3. Equation (4.4) can also be derived by letting the bending rigidity $K \rightarrow 0^+$ in Donnell's. Specifically, writing Eq. (4.8) as

$$K \frac{d^4 u_r}{dz^4} + \frac{Et}{a^2} u_r = (1 - \nu/2)p(z) \quad (4.15)$$

makes the limit obvious. This observation shows that, in the limit of negligible bending, the shell theory reduces to the membrane theory self-consistently.

5. Coupling the fluid mechanics and structural problems: Flow rate–pressure drop relation

We now turn to the main task, which is evaluating the pressure drop as function of the flow rate and thus generalizing the Hagen–Poiseuille law to deformable microtubes. The flow rate in the pipe is by definition

$$q = \int_0^{2\pi} \int_0^{R(z)} v_z r dr d\theta = \mathcal{V}_z 2\pi a^2 \int_0^{\bar{R}(\bar{z})} \bar{v}_{\bar{z}} \bar{r} d\bar{r}, \quad (5.1)$$

where the second equality follows from performing the (trivial) azimuthal integration and introducing the dimensionless variables from Eq. (5.33) and the corresponding change in integration limits. Now, substituting the expression for $\bar{v}_{\bar{z}}$ from Eq. (3.13) into the latter:

$$\begin{aligned} q &= \mathcal{V}_z 2\pi a^2 \int_0^{\bar{R}(\bar{z})} \left(-\frac{1}{2} \frac{d\bar{p}}{d\bar{z}} \right)^{1/n} \frac{[\bar{R}(\bar{z})]^{1+1/n} - \bar{r}^{1+1/n}}{1+1/n} \bar{r} d\bar{r} \\ &= \mathcal{V}_z \pi a^2 \left(-\frac{1}{2} \frac{d\bar{p}}{d\bar{z}} \right)^{1/n} \frac{[\bar{R}(\bar{z})]^{3+1/n}}{3+1/n}. \end{aligned} \quad (5.2)$$

Henceforth, we use the dimensionless flow rate $\bar{q} = q/(\mathcal{V}_z \pi a^2)$. In a steady flow, conservation of mass requires that q is a constant independent of z , thus Eq. (5.2) is an ODE for $\bar{p}(\bar{z})$, subject to an appropriate closure relation for $\bar{R}(\bar{z})$.

5.1. Rigid tube

First, for completeness and future reference, consider the case of $\bar{R} = 1$ (rigid tube of uniform radius). Equation (5.2) can be immediately integrated to yield the usual linear pressure profile

$$\bar{p}(\bar{z}) = 2[(3 + 1/n)\bar{q}]^n(1 - \bar{z}). \quad (5.3)$$

Since it is our convention that $\bar{p}(\bar{z} = 0) = \Delta\bar{p}$ is the full pressure drop across the microtube, then

$$\Delta\bar{p} = 2[(3 + 1/n)\bar{q}]^n, \quad (5.4)$$

which is the well-known *Hagen–Poiseuille law for a power-law fluid* (Bird *et al.* 1987).

5.2. Leading-order-in-thickness shell theory

Next, inserting the relation $\bar{R} = 1 + (1 - \nu/2)\beta\bar{p}$ [having employed Eqs. (4.13) and (4.14)] into Eq. (5.2) yields an ordinary differential equation (ODE) for $\bar{p}(\bar{z})$ given \bar{q} :

$$\frac{d\bar{p}}{d\bar{z}} = -2[(3 + 1/n)\bar{q}]^n[1 + (1 - \nu/2)\beta\bar{p}]^{-(3n+1)}. \quad (5.5)$$

Separating variables and integrating, subject to the outlet boundary condition $[\bar{p}(1) = 0]$ we have:

$$\bar{q}^n(\bar{z} - 1) = \frac{1 - [1 + (1 - \nu/2)\beta\bar{p}]^{3n+2}}{2(3 + 1/n)^n(3n + 2)(1 - \nu/2)\beta}. \quad (5.6)$$

Equation (5.6) is an *implicit* relation for the pressure (given \bar{q}), which (unlike the case of microchannels (Christov *et al.* 2018; Shidhore & Christov 2018; Anand *et al.* 2018)) can be inverted to yield

$$\bar{p}(\bar{z}) = \frac{1}{(1 - \nu/2)\beta} \left\{ [1 - 2(3n + 2)(1 - \nu/2)\beta[(3 + 1/n)\bar{q}]^n(\bar{z} - 1)]^{1/(3n+2)} - 1 \right\}. \quad (5.7)$$

The flow rate–pressure drop relation is obtained by evaluating Eq. (5.6) at $\bar{z} = 0$:

$$\bar{q} = \left(\frac{1}{2(3 + 1/n)^n(3n + 2)(1 - \nu/2)\beta} \left\{ [1 + (1 - \nu/2)\beta\Delta\bar{p}]^{(3n+2)} - 1 \right\} \right)^{1/n}. \quad (5.8)$$

REMARK 4. Equation (5.5) can be inverted to yield the flow rate in terms of the pressure gradient:

$$\bar{q} = \sigma(\bar{p}) \left(-\frac{d\bar{p}}{d\bar{z}} \right)^{1/n}, \quad \sigma(\bar{p}) := \frac{1}{3 + 1/n} \left\{ \frac{1}{2} [1 + (1 - \nu/2)\beta\bar{p}]^{(3n+1)} \right\}^{1/n}. \quad (5.9a, b)$$

The form of this equation is, clearly, a generalization of the classic result of Rubinow & Keller (1972) for steady low Re , Newtonian flow in a deformable tube. More importantly, however, we have also self-consistently derived the function σ that accounts for steady non-Newtonian FSI in a microtube.

REMARK 5. The maximum deflection of the microtube wall over its length [recall Eq. (4.13)] is given by $\beta\bar{u}_{\bar{r}}(\bar{0})$, which can be re-expressed, via Eq. (4.14), as $(1 - \nu/2)\beta\bar{p}(0)$. Now, $\bar{p}(0)$ can be inserted from Eq. (5.7) to ultimately yield, under the leading-order-in-thickness theory,

$$\max_{0 \leq \bar{z} \leq 1} \beta\bar{u}_{\bar{r}}(\bar{z}) = \left\{ [1 + 2(3n + 2)(1 - \nu/2)\beta[(3 + 1/n)\bar{q}]^n]^{1/(3n+2)} - 1 \right\}. \quad (5.10)$$

Note that, once the solid and fluid properties (ν and n) are fixed, the maximum deflection is solely a function of the dimensionless flow rate \bar{q} and the FSI parameter β . The maximum deflection thus calculated is higher for shear-thinning fluids compared to shear-thickening fluids, except at low values of β . The complex interplay of β and n is discussed more thoroughly in §6 and in Appendix B.

REMARK 6. To perform the consistency check of recovering the rigid-tube pressure profile in Eq. (5.3) as the $\beta \rightarrow 0^+$ limit of the deformable-tube pressure profile in Eq. (5.7), we must realize that $\beta \rightarrow 0^+$ in Eq. (5.7) is a “0/0” limit. L’Hôpital’s rule or a Taylor series in $\beta \ll 1$ easily shows that Eq. (5.3) is indeed the $\beta \rightarrow 0^+$ limit of Eq. (5.7).

5.2.1. Special case of FSI in a microtube due to flow of a Newtonian fluid

Now, let us consider the case of a Newtonian fluid (i.e., $n = 1$ and $m = \mu$) of Eq. (5.7):

$$\bar{p}(\bar{z}) = \frac{1}{(1 - \nu/2)\beta} \left\{ [1 - 40(1 - \nu/2)\beta\bar{q}(\bar{z} - 1)]^{1/5} - 1 \right\}. \quad (5.11)$$

Meanwhile, from Eq. (5.8), we have

$$\bar{q} = \frac{1}{40(1 - \nu/2)\beta} \left\{ [1 + (1 - \nu/2)\beta\Delta\bar{p}]^5 - 1 \right\}. \quad (5.12)$$

It is instructive to compare our thus obtained flow rate–pressure drop relation for Newtonian fluids, i.e., Eq. (5.12), to the corresponding relation in Fung’s classic *Biomechanics* textbook (Fung 1997, §3.4), which is often quoted in newer texts on biofluid mechanics as well (Ayyaswamy 2016, pp. e25–e27).

The most obvious difference is that, in (Fung 1997, §3.4, Eq. (8)) the flow rate depends upon the pressure drop to the third power, while in Eq. (5.12) the flow rate depends upon pressure drop to fifth power. This nontrivial difference is attributed to conflicting assumptions made about the elasticity problem. Fung (Fung 1997, §3.4), assumes that the hoop stress can be written in terms of the tube’s *deformed* radius (Fung 1997, §3.4, Eq. (3)), while we have defined the hoop stress (and normal stress resultant) in terms of the tube’s *undeformed* radius [see Eqs. (4.1a) and (4.2)]. In doing so, we were able to formulate relationships between stress resultants and displacements using shell theory. Then, the deformed radius and stress in the deformed tube can be obtained without extra assumptions. In other words, Fung’s approach is suitable for thin circular slices that inflate like a balloon. On the other hand, the theory developed herein is suitable for modeling long, slender microtubes. Moreover, both Fung’s and our theory hinge upon the assumption of linear (small strain) elasticity. As we discuss below, the range of applicability of this “linear” FSI theory is for large pressure but small pressure gradient. Conceivably, this is only possible in long microtubes ($\ell \gg a$), where Fung’s example’s assumptions are invalid.

REMARK 7. *In the limit of no FSI, i.e., $\beta \rightarrow 0^+$, we may again perform a Taylor series expansion in $\beta \ll 1$ starting from Eq. (5.11) to obtain $\bar{p}(\bar{z}) = 8\bar{q}(1 - \bar{z})$. The latter, of course, yields the dimensionless Hagen–Poiseuille law on evaluating it at $\bar{z} = 0$.*

5.3. Beyond leading-order-in-thickness shell theory

In §5.2, we obtained the flow rate–pressure drop relationship considering only the leading-order deformation profile as given by Eq. (4.4). In this subsection, we venture beyond the leading-order approximation by solving the “full” ODE (4.8) for the deformation under Donnell’s shell theory. Equation (4.8) is coupled to Eq. (5.2), which expresses the pressure gradient in terms of the flow rate (or *vice versa*).

For clarity, we start from the dimensional equations and non-dimensionalize. Equation (5.2), in dimensional variables can be expressed, as

$$\frac{dp}{dz} = \left[\frac{(3 + 1/n)q}{\pi} \right]^n \left[\frac{-2m}{(a + u_r)^{3n+1}} \right]. \quad (5.13)$$

Next, taking d/dz of Eq. (4.8) and substituting Eq. (5.13) into the latter yields a single *nonlinear* fifth-order ODE in the deformation:

$$\frac{Et^3}{12(1 - \nu^2)}(a + u_r)^{3n+1} \left[\frac{d^5 u_r}{dz^5} + \frac{12(1 - \nu^2)}{a^2 t^2} \frac{du_r}{dz} \right] = (-2m) \left[\frac{(3 + 1/n)q}{\pi} \right]^n (1 - \nu/2). \quad (5.14)$$

The dimensionless form of Eq. (5.14), using the variables previously defined in Eq. (4.9), is

$$(1 + \beta \bar{u}_{\bar{r}})^{3n+1} \left[\underbrace{\left(\frac{t}{a} \right)^2 \left(\frac{a}{\ell} \right)^4 \frac{d^5 \bar{u}_{\bar{r}}}{d\bar{z}^5}}_{\text{bending}} + \underbrace{12(1 - \nu^2) \frac{d\bar{u}_{\bar{r}}}{d\bar{z}}}_{\text{stretching}} \right] = -24(1 - \nu^2)(1 - \nu/2)[(3 + 1/n)\bar{q}]^n. \quad (5.15)$$

loading

The ODE in Eq. (5.15) is subject to the following boundary conditions expressing clamping of the shell at the inlet and outlet planes (Eqs. (5.16a) and (5.16b), respectively) and zero gage pressure at the outlet (Eq. (5.16c)):

$$\bar{u}_{\bar{r}}|_{\bar{z}=0} = \frac{d\bar{u}_{\bar{r}}}{d\bar{z}} \Big|_{\bar{z}=0} = 0, \quad (5.16a)$$

$$\bar{u}_{\bar{r}}|_{\bar{z}=1} = \frac{d\bar{u}_{\bar{r}}}{d\bar{z}} \Big|_{\bar{z}=1} = 0, \quad (5.16b)$$

$$\frac{d^4 \bar{u}_{\bar{r}}}{d\bar{z}^4} \Big|_{\bar{z}=1} = 0. \quad (5.16c)$$

Equations (5.15) and (5.16) represent a nonlinear *two-point boundary value problem* (BVP) (Keller 1976), the solution of which fully characterizes the physics of FSI in microtube conveying a non-Newtonian fluid within.

This theory is based upon the assumptions of slenderness ($\ell \ll a$) and thinness ($t \ll a$). Therefore, in the limit of vanishing t/a and a/ℓ , Eq. (5.15) becomes an example of a *singular perturbation problem*. Physically, “boundary layers” develop near the inlet and outlet of the microtube where the bending due to clamping becomes significant. As a singular perturbation problem, Eq. (5.15) is now amenable to treatment via *matched asymptotics* (Holmes 2013, Ch. 2).

To that end, we introduce a dimensionless small parameter $\epsilon = \sqrt{ta/\ell^2} \ll 1$, then Eq. (5.15) can be rewritten as:

$$(1 + \beta \bar{u}_{\bar{r}})^{3n+1} \left[\epsilon^4 \frac{d^5 \bar{u}_{\bar{r}}}{d\bar{z}^5} + 12(1 - \nu^2) \frac{d\bar{u}_{\bar{r}}}{d\bar{z}} \right] = -24(1 - \nu^2)(1 - \nu/2)[(3 + 1/n)\bar{q}]^n. \quad (5.17)$$

As is standard, we first let $\epsilon \rightarrow 0^+$, thus singularly perturbing the ODE, and obtain the governing equation for the solution in the *outer region*:

$$(1 + \beta \bar{u}_{\bar{r}})^{3n+1} \frac{d\bar{u}_{\bar{r}}}{d\bar{z}} = -2(1 - \nu/2)[(3 + 1/n)\bar{q}]^n. \quad (5.18)$$

The outer solution must “respect” the outlet pressure boundary condition [i.e., $\bar{p}(\bar{z} = 1) = 0$], which can be identified as the first part of the clamping condition at $\bar{z} = 1$, i.e., $\bar{u}_{\bar{r}}|_{\bar{z}=1} = 0$ from Eq. (5.16b). Then, the solution to Eq. (5.18) is

$$\bar{u}_{\bar{r}}(\bar{z}) = \frac{1}{\beta} \left(\{1 + 2\beta(3n+2)(1 - \nu/2)[(3 + 1/n)\bar{q}]^n(1 - \bar{z})\}^{1/(3n+2)} - 1 \right). \quad (5.19)$$

Note that Eq. (5.19) can also be obtained by combining Eqs. (4.14) and (5.7) from the membrane theory, showing the consistency of our two structural mechanics models.

To satisfy the clamped boundary condition at $\bar{z} = 0$, i.e., Eq. (5.16a), we must introduce a *boundary layer* near $\bar{z} = 0$ wherein the highest-order derivative in Eq. (5.17) are dominant and are retained. Then, an inner solution can be obtained. To this end, we

introduce a scaled spatial coordinate ζ such that for $\bar{z} \ll 1$, $\zeta = \mathcal{O}(1)$. A straightforward balancing argument leads us to define $\zeta = \bar{z}/\epsilon$. Then, the nonlinear ODE (5.17) becomes

$$\frac{d^5\bar{u}_{\bar{r}}}{d\zeta^5} + 12(1-\nu^2)\frac{d\bar{u}_{\bar{r}}}{d\zeta} = \epsilon \left\{ \frac{-24(1-\nu^2)(1-\nu/2)[(3+1/n)\bar{q}]^n}{(1+\beta\bar{u}_{\bar{r}})^{3n+1}} \right\}. \quad (5.20)$$

At the leading order in $\epsilon \ll 1$, we have

$$\frac{d^5\bar{u}_{\bar{r}}}{d\zeta^5} + 12(1-\nu^2)\frac{d\bar{u}_{\bar{r}}}{d\zeta} = 0 \quad (5.21)$$

subject to the following boundary conditions:

$$\bar{u}_{\bar{r}}|_{\zeta=0} = \frac{d\bar{u}_{\bar{r}}}{d\zeta}\bigg|_{\zeta=0} = 0, \quad (5.22a)$$

$$\bar{u}_{\bar{r}}|_{\zeta \rightarrow \infty} = \bar{u}_{\bar{r}}^{\text{outer}}|_{\bar{z}=0}, \quad (5.22b)$$

where $\bar{u}_{\bar{r}}^{\text{outer}}$ denotes the outer solution from Eq. (5.19). Here, the first two boundary conditions (at $\zeta = 0$) are due to clamping, while the remaining boundary condition (as $\zeta \rightarrow \infty$) is necessary to *match* the inner solution to the outer solution.

Next, we integrate Eq. (5.21) once to obtain

$$\frac{d^4\bar{u}_{\bar{r}}}{d\zeta^4} + 12(1-\nu^2)\bar{u}_{\bar{r}} = C_0, \quad (5.23)$$

where C_0 is a (yet) unknown integration constant. The solution of Eq. (5.23) consists of a homogeneous solution $\bar{u}_{\bar{r},H}$ and a particular solution $\bar{u}_{\bar{r},P}$. The homogeneous part of the ODE (5.23) has the characteristic polynomial $r_i^4 = -12(1-\nu^2)$, the four complex roots of which are easily found, thus

$$\begin{aligned} \bar{u}_{\bar{r},H}(\zeta) = & C_1 e^{(1+i)\sqrt[4]{3(1-\nu^2)}\zeta} + C_2 e^{-(1+i)\sqrt[4]{3(1-\nu^2)}\zeta} \\ & + C_3 e^{(1-i)\sqrt[4]{3(1-\nu^2)}\zeta} + C_4 e^{-(1-i)\sqrt[4]{3(1-\nu^2)}\zeta}. \end{aligned} \quad (5.24)$$

Now, since $\bar{u}_{\bar{r},H}$ must remain bounded as $\zeta \rightarrow \infty$, we require that $C_1, C_3 = 0$. The particular solution is easily found to be

$$\bar{u}_{\bar{r},P}(\zeta) = \frac{C_0}{12(1-\nu^2)}. \quad (5.25)$$

Therefore, the general solution, $\bar{u}_{\bar{r}} = \bar{u}_{\bar{r},H} + \bar{u}_{\bar{r},P}$, to Eq. (5.23) is

$$\bar{u}_{\bar{r}}(\zeta) = C_2 e^{-(1+i)\sqrt[4]{3(1-\nu^2)}\zeta} + C_4 e^{-(1-i)\sqrt[4]{3(1-\nu^2)}\zeta} + \frac{C_0}{12(1-\nu^2)}. \quad (5.26)$$

Before applying the boundary conditions, we redefine the arbitrary constants of integration C_1 and C_2 to be $\tilde{C}_4 = C_4 + C_2$ and $\tilde{C}_2 = (C_4 - C_2)i$. Then, the real-valued solution to Eq. (5.23) can be expressed as

$$\bar{u}_{\bar{r}}(\zeta) = e^{-\zeta\sqrt[4]{3(1-\nu^2)}} \left[\tilde{C}_2 \sin \left(\zeta \sqrt[4]{3(1-\nu^2)} \right) + \tilde{C}_4 \cos \left(\zeta \sqrt[4]{3(1-\nu^2)} \right) \right] + \frac{C_0}{12(1-\nu^2)}, \quad (5.27)$$

Now, we apply the boundary condition $\bar{u}_{\bar{r}}|_{\zeta=0} = 0$ to obtain:

$$\tilde{C}_4 + \frac{C_0}{12(1-\nu^2)} = 0. \quad (5.28)$$

Next, we use the boundary condition $(d\bar{u}_r/d\zeta)|_{\zeta=0} = 0$ to find that $\tilde{C}_2 = \tilde{C}_4$. Finally, from the matching condition in Eq. (5.22b), we find

$$\tilde{C}_4 = \frac{1}{\beta} \left(1 - \left\{ 1 + 2\beta(3n+2)(1-\nu/2)[(3+1/n)\bar{q}]^n \right\}^{1/(3n+2)} \right). \quad (5.29)$$

Thus, the final expression for the inner solution in the boundary layer near $\bar{z} = 0$ is

$$\bar{u}_r(\zeta) \sim \tilde{C}_4 \left\{ e^{-\zeta \sqrt[4]{3(1-\nu^2)}} \left[\sin \left(\zeta \sqrt[4]{3(1-\nu^2)} \right) + \cos \left(\zeta \sqrt[4]{3(1-\nu^2)} \right) \right] - 1 \right\} \quad (5.30)$$

to the leading order in ϵ .

Next, another boundary layer must exist near the outlet at $\bar{z} = 1$ because, although $\bar{u}_r^{\text{outer}} \rightarrow 0$ as $\bar{z} \rightarrow 1$, $d\bar{u}_r^{\text{outer}}/d\bar{z} \not\rightarrow 0$ as $\bar{z} \rightarrow 1$, i.e., the clamping boundary condition is not fully satisfied. Thus, we expect both the dependent (deformation) and the independent (axial position) variables to be small in this layer. That is, we conjecture that the boundary layer at $\bar{z} = 1$ is actually a *corner layer* (Holmes 2013, §2.6) (sometimes termed a derivative layer (see Neu 2015, pp. 85–93)). As is customary in matched asymptotics, it is our duty now to substantiate this hypothesis. Before we begin, it is also relevant to mention the matched asymptotic solution for a *moving* elastohydrodynamic front given in (Elbaz & Gat 2016, §4.2), which it should be noted works somewhat differently in the unsteady problem.

Now, introducing the rescalings $\zeta = (1 - \bar{z})/\epsilon^{\alpha_1}$ and $\hat{u}(\zeta) = \bar{u}_r(\bar{z})/\epsilon^{\alpha_2}$ into Eq. (5.17), we can balance all three terms if and only if $\alpha_1 = \alpha_2 = 1$. The first and last terms can be balanced for any $4 - 5\alpha_1 + \alpha_2 = 0$ as long as $\alpha_1 < \alpha_2$ but then there is a non-uniqueness of the boundary layer thickness, so we discard this possibility. Then, the nonlinear ODE (5.17) becomes

$$\frac{d^5\hat{u}}{d\zeta^5} + 12(1-\nu^2) \frac{d\hat{u}}{d\zeta} = \frac{24(1-\nu^2)(1-\nu/2)[(3+1/n)\bar{q}]^n}{(1+\beta\epsilon\hat{u})^{3n+1}}. \quad (5.31)$$

Then, expanding in $\epsilon \ll 1$, we have at the leading order:

$$\frac{d^5\hat{u}}{d\zeta^5} + \mathcal{A}_1 \frac{d\hat{u}}{d\zeta} = \mathcal{A}_2, \quad (5.32)$$

where for convenience we have defined

$$\mathcal{A}_1 := 12(1-\nu^2), \quad \mathcal{A}_2 := 24(1-\nu^2)(1-\nu/2)[(3+1/n)\bar{q}]^n. \quad (5.33a, b)$$

The ODE (5.32) must satisfy the remaining boundary conditions at $\bar{z} = 1$, from Eqs. (5.16b) and (5.16c), that are not satisfied by the outer solution, namely

$$\frac{d\hat{u}}{d\zeta} \Big|_{\zeta=0} = \frac{d^4\hat{u}}{d\zeta^4} \Big|_{\zeta=0} = 0, \quad (5.34a)$$

$$\hat{u} \Big|_{\zeta \rightarrow \infty} = \bar{u}_r^{\text{outer}} \Big|_{\bar{z}=1}. \quad (5.34b)$$

For a corner layer, the matching condition in Eq. (5.34b) is a bit “trickier” and is implemented using an intermediate variable technique (Holmes 2013, §2.6).

The particular solution of Eq. (5.32) is $\hat{u}_P = \mathcal{A}_2\zeta/\mathcal{A}_1$. The homogeneous \hat{u}_H solution of Eq. (5.32) satisfies

$$\frac{d^4\hat{u}_H}{d\zeta^4} + \mathcal{A}_1 \hat{u}_H = C_0. \quad (5.35)$$

The solution of the latter ODE, implementing the decay for $\zeta \rightarrow \infty$, as above, is

$$\hat{u}_H(\zeta) = e^{-\zeta \sqrt[4]{3(1-\nu^2)}} \left[\tilde{C}_2 \sin \left(\zeta \sqrt[4]{3(1-\nu^2)} \right) + \tilde{C}_4 \cos \left(\zeta \sqrt[4]{3(1-\nu^2)} \right) \right] + \frac{C_0}{\mathcal{A}_1}. \quad (5.36)$$

Thus, we obtain the solution to Eq. (5.32) as

$$\hat{u}(\zeta) = \frac{\mathcal{A}_2}{\mathcal{A}_1} \zeta + e^{-\zeta \sqrt[4]{3(1-\nu^2)}} \left[\tilde{C}_2 \sin \left(\zeta \sqrt[4]{3(1-\nu^2)} \right) + \tilde{C}_4 \cos \left(\zeta \sqrt[4]{3(1-\nu^2)} \right) \right] + \frac{C_0}{\mathcal{A}_1}, \quad (5.37)$$

Now, we impose the boundary condition $(d\hat{u}/d\zeta)|_{\zeta=0} = 0$ to find that

$$\frac{\mathcal{A}_2}{\mathcal{A}_1} + \sqrt[4]{3(1-\nu^2)}(\tilde{C}_2 - \tilde{C}_4) = 0 \quad \Rightarrow \quad \tilde{C}_2 = \tilde{C}_4 - \frac{\mathcal{A}_2}{\mathcal{A}_1 \sqrt[4]{3(1-\nu^2)}}. \quad (5.38)$$

Finally, the boundary condition $(d^4\hat{u}/d\zeta^4)|_{\zeta=0} = 0$ requires that $\tilde{C}_4 = 0$. Thus, we have obtained a fully-specified corner layer (inner) solution:

$$\hat{u}(\zeta) \sim \frac{\mathcal{A}_2}{\mathcal{A}_1} \left[\zeta - \frac{e^{-\zeta \sqrt[4]{3(1-\nu^2)}}}{\sqrt[4]{3(1-\nu^2)}} \sin \left(\zeta \sqrt[4]{3(1-\nu^2)} \right) \right] + \frac{C_0}{\mathcal{A}_1}. \quad (5.39)$$

The inner solution in Eq. (5.39) must still be matched to the outer solution in Eq. (5.19), which goes to zero as $\bar{z} \rightarrow 1$. Thus, we immediately conclude that $C_0 = 0$, and the common part of the inner and outer solutions is $\mathcal{A}_2\zeta/\mathcal{A}_1$ [as can be confirmed by a Taylor series expansion of Eq. (5.19) for $\bar{z} \approx 1$]. This argument can also be made even more rigorous using an intermediate variable matching procedure as in (Holmes 2013, §2.6).

Finally, adding together Eqs. (5.19), (5.30) and (5.39) (expressed in the original variables) and subtracting their mutual common parts, we obtain a *composite solution* uniformly valid on $\bar{z} \in [0, 1]$, to the leading order in ϵ :

$$\begin{aligned} \bar{u}_{\bar{r}}(\bar{z}) \sim & \frac{1}{\beta} \left(\{1 + 2\beta(3n+2)(1-\nu/2)[(3+1/n)\bar{q}]^n(1-\bar{z})\}^{1/(2+3n)} - 1 \right) \\ & + \tilde{C}_4 e^{-\sqrt[4]{3(1-\nu^2)}\bar{z}/\epsilon} \left[\sin \left(\sqrt[4]{3(1-\nu^2)} \frac{\bar{z}}{\epsilon} \right) + \cos \left(\sqrt[4]{3(1-\nu^2)} \frac{\bar{z}}{\epsilon} \right) \right] \\ & - \epsilon \frac{2(1-\nu/2)[(3+1/n)\bar{q}]^n}{\sqrt[4]{3(1-\nu^2)}} e^{-\sqrt[4]{3(1-\nu^2)}(1-\bar{z})/\epsilon} \sin \left(\sqrt[4]{3(1-\nu^2)} \frac{(1-\bar{z})}{\epsilon} \right), \end{aligned} \quad (5.40)$$

where the constant \tilde{C}_4 is given in Eq. (5.29).

6. Results and discussion

6.1. Deviations from the ideal Hagen–Poiseuille law due to FSI

Our ultimate objective is to understand, predict and quantify the deviations, caused by FSI in a microtube, from the ideal Hagen–Poiseuille law. To this end, we must evaluate the effects of two competing physical mechanisms: (i) the non-Newtonian rheology of the fluid (quantified via power-law index n), and (ii) the compliance of the microtube’s wall (quantified via the FSI parameter β). On the one hand, the viscous stresses in the fluid increase with n (the fluid’s resistance to flow increases), which leads to a larger pressure drop for a fixed inlet flow rate. On the other hand, the effective cross-sectional area of the flow conduit increases with β (large tube deformation), thereby reducing the resistance to flow and the pressure drop at a fixed inlet flow rate. Thus, there is a non-

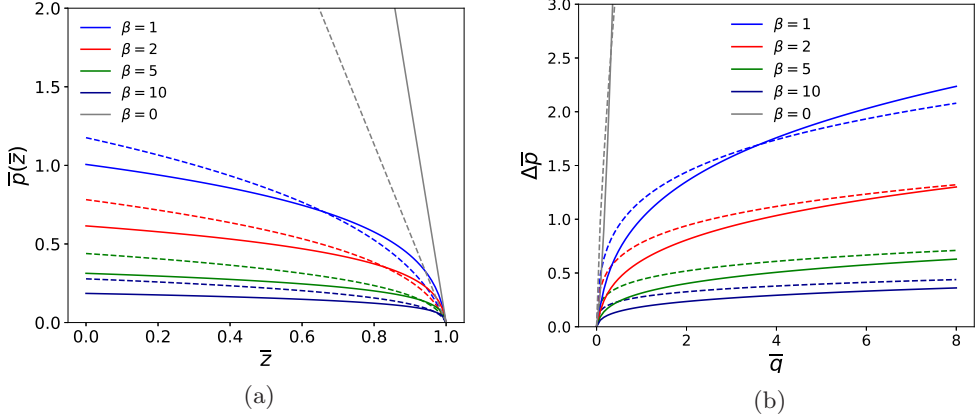


Figure 2: (a) The dimensionless hydrodynamic pressure \bar{p} in a microtube as a function of the dimensionless axial coordinate \bar{z} for different values of the FSI parameter β with $\bar{q} = 1$. (b) Full dimensionless pressure drop $\Delta\bar{p}$ across a microtube as a function of the dimensionless flow rate \bar{q} for different values of β . Both plots have been produced using Eq. (5.7). The dashed and solid curves represent a shear-thinning ($n = 0.7$) and a shear-thickening fluid ($n = 1.5$), respectively. Note the different vertical scales in panels (a) and (b).

trivial interplay of shear-dependent viscosity and tube wall compliance as we now discuss and as is shown with due mathematical rigor in Appendix B.

First, consider Fig. 2(a), which shows the pressure profile, $\bar{p}(\bar{z})$, along the length of the microtube. We immediately recognize that, due to FSI, the pressure profile is not linear in \bar{z} , as previously discussed in (Christov *et al.* 2018; Shidhore & Christov 2018). More importantly, we see that for lower values of β , the shear-thickening fluids (solid lines, $n > 1$) sustain higher pressure throughout the tube compared to shear-thinning fluids (dashed lines, $n < 1$). However, for higher values of β , the trend is reversed and the shear-thinning fluids support higher pressure. This is clearly a manifestation of the competition of physical effects discussed in the previous paragraph. Overall, however, it is worth observing that the maximum pressure in the presence of non-Newtonian FSI ($\beta \neq 0$ and $n \neq 1$) is *significantly* reduced compared to flow of a rigid tube ($\beta = 0$, gray curves).

Next, in Fig. 2(b) we show the full (dimensionless) pressure drop $\Delta\bar{p}$ as a function of the flow rate \bar{q} for different values of β . Trends similar to Fig. 2(a) are observed, and $\Delta\bar{p}$ is higher for shear-thinning fluids, except at low values of β , for which the shear-thickening fluids cause a higher $\Delta\bar{p}$. We note that the non-linear relationship between pressure drop and flow rate exists for rigid walls ($\beta = 0$) as well (gray curves), as is well established in textbooks (Bird *et al.* 1987) and also shown by Eq. (5.4), even if not so obvious due to the scales in Fig. 2(b). Once again, we conclude by noting that $\Delta\bar{p}$ is *very significantly* reduced by FSI.

6.2. Comparison between analytical and numerical solutions

Our results in §5, suggest the following possible ways for solving the coupled problem of coupled flow and deformation in an elastic tube: (i) using leading-order-in-thickness membrane theory method (§5.2), (ii) using the a matched asymptotic expansion for

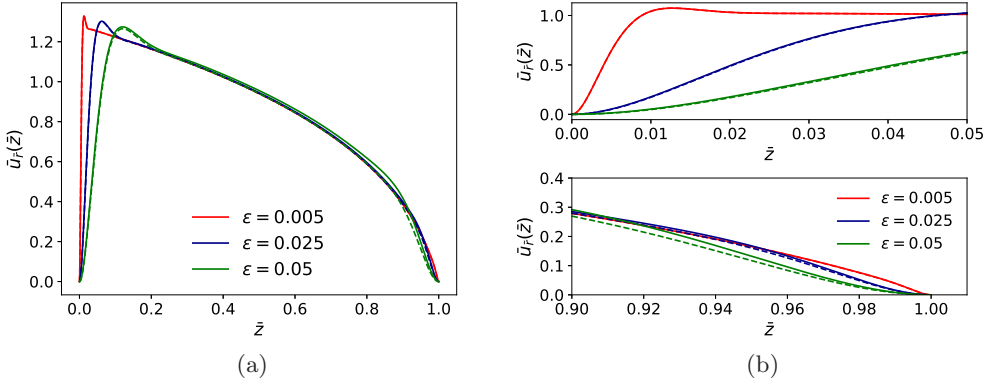


Figure 3: The dimensionless radial deflection $\bar{u}_r(\bar{z})$ as a function of the dimensionless axial position \bar{z} in the microtube for $\beta = 1$, $n = 0.7$, $\bar{q} = 2$ and $\nu = 1/2$. The solid curves are the numerical solution of TPBVP given by Eqs. (5.15) and (5.16), while dashed curves are matched asymptotic solution, namely Eq. (5.40). Panel (a) shows the deflection over the whole tube, while panels (b) and (c) show zoom-ins of near the clamped ends. In most cases the agreement between the numerical and asymptotic solutions is so good that they are difficult to distinguish.

beyond-leading-order-in-thickness (i.e., Donnell shell) theory to capture bending and clamping (§5.3), and (iii) by numerical integration of the nonlinear ODE for the displacement obtained in §5.3. We may conceptualize these approaches as a hierarchy: the leading-order perturbative solution is a less accurate version of solution obtained by the matched asymptotic expansion, while the the matched asymptotic expansion is a less accurate version of the solution found by numerically integrating the ODE.

Let us now compare the deformation profile obtained via matched asymptotics, i.e., Eq. (5.40) to the numerical solution of the original nonlinear two-point BVP. The latter is obtained using the `solve_bvp` subroutine in Python's SciPy module (Jones *et al.* 2001). Figure 3 shows the results of such a comparison for different values of the small parameter $\epsilon = \sqrt{ta/\ell^2}$ but fixed β , n , \bar{q} and ν . We see that there is very good agreement between the composite solution obtained via a matched asymptotic expansion and the numerical solution of the nonlinear fifth-order ODE (5.15). As expected, the error in the composite solution increase with ϵ , especially in the corner layer at $\bar{z} = 1$, nevertheless the asymptotic expression is clearly highly accurate.

In addition, we observe that the axial displacement profile, exhibits an overshoot near the inlet due to clamping, which is not the case for a two-dimensional plate top wall in a soft microchannel Christov *et al.* (2018); Shidhore & Christov (2018); Anand *et al.* (2018). This complex feature of the displacement profile, along with the corner layer at the outlet, are accurately captured by the match asymptotic solution given in Eq. (5.40).

6.3. Comparison between theory and direct numerical simulations

To ascertain the validity of the theory developed in this paper, we now compare our theoretical results against three-dimensional (3D) direct numerical simulations (DNS) of coupled flow and deformation in a microtube. To this end, we choose an illustrative set of physical and geometric parameters, as given in Table 1. The dimensions have been chosen to ensure that the assumptions of slenderness and shallowness are satisfied. The

a (mm)	ℓ (mm)	a/ℓ	t (mm)	t/a	E (MPa)	ν	μ (Pa·s)	n	m (Pa·s n)	ρ (kg/m 3)
0.08	3.2	0.025	0.008	0.1	0.5	0.499	0.0012	0.7	0.0185	1,060

Table 1: Geometric and material properties for a sample microtube FSI problem.

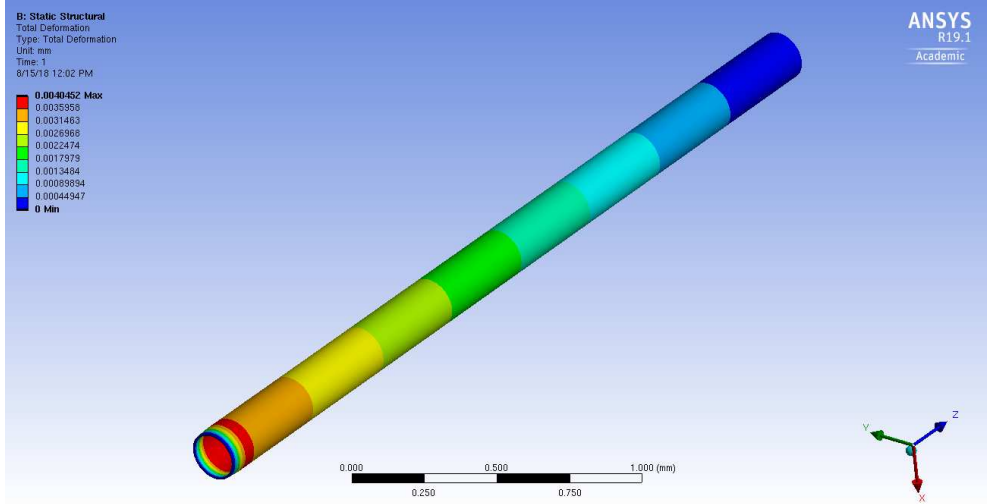


Figure 4: Microtube in its deformed state, as computed by the ANSYS FSI simulation.

microtube is assumed to be made of elastin, which is a highly elastic protein found in all vertebrates and is major constituent of arteries, where it enables pressure wave propagation and transport through blood vessels (Sandberg *et al.* 1977). Here, elastin is modeled as an isotropic linearly elastic solid with a constant Young's modulus of $E = 0.5$ MPa and a Poisson ratio of $\nu = 0.499$ (i.e., a nearly incompressible material), along the lines of the work in (Sandberg *et al.* 1977; Matsumoto *et al.* 2015; Ebrahimi 2009). The generalized Newtonian fluid inside the microtube is assumed to be human blood. Blood rheology is a topic of active research, as the rheological properties of blood depend on various factors such as a patient's age, health, concentration of plasma, etc. (Hussain *et al.* 1999; Chakraborty 2005). Here, for the sake of simplicity, and without sacrificing any physics, and to validate our theory for both Newtonian and non-Newtonian rheologies, blood plasma is chosen our example Newtonian fluid with constant shear viscosity of $\mu = 0.0012$ Pa·s (i.e., $m = \mu$ and $n = 1$) (Fung 1997), while whole blood is chosen as our example shear-thinning fluid with a power-law index of $n = 0.7$ and a consistency index of $m = 0.0185$ Pa·s n (Hussain *et al.* 1999). In both cases, a density of $\rho = 1,060$ kg/m 3 is used, which is within the range for both blood plasma and whole blood (see, e.g., Kleinstreuer 2006, Table 2.1.1). Simulations were carried out for flow rates up to $q = 2.00$ mL/min, which correspond to a maximum $Re \approx 150$.

For our computational approach, we employ a segregated solution strategy, as opposed to a monolithic one (see, e.g., Bazilevs *et al.* 2013). That is, the solid (resp. fluid) problem is solved independently of the fluid (resp. solid) problem, each on its own computational domain. The displacements (resp. forces) from the solid (resp. fluid) domain are then transferred to the fluid (resp. solid) domain via a surface traction

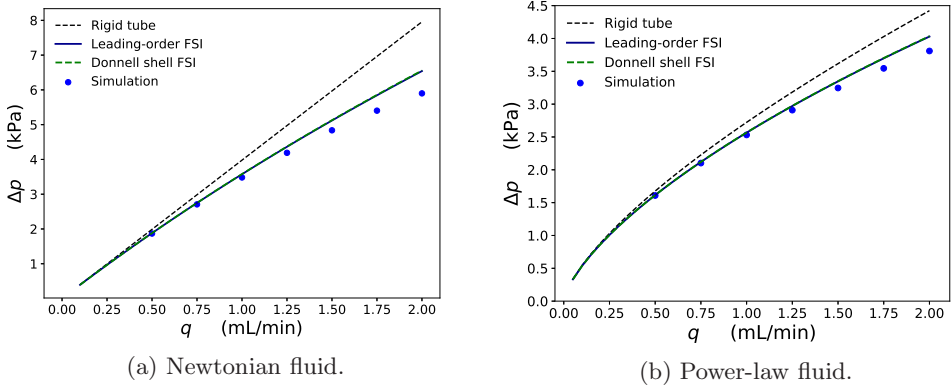


Figure 5: Pressure drop vs. flow rate in a deformable microtube. Fluid–structure interaction causes the pressure drop to decrease in the deformable tube compared to the rigid one. The perturbative analysis developed herein, culminating in Eqs. (5.8) [power-law, (b)] and (5.12) [Newtonian, (a)] captures the latter effect quite accurately, when compared to 3D direct numerical simulations. The leading-order FSI and the Donnell shell FSI curves are nearly identical in both panels. Note the different vertical scales in panels (a) and (b).

boundary condition. Based on previous successful computational microscale FSI studies (Chakraborty *et al.* 2012; Shidhore & Christov 2018; Anand *et al.* 2018), we have used the commercial computer-aided engineering (CAE) software from ANSYS Inc. (2018) to perform such two-way coupled FSI DNS via a segregated approach. The geometry was created in ANSYS SpaceClaim, and the mesh was generated in ANSYS ICEM CFD. The steady incompressible mass and momentum equations for the power-law fluid were solved using ANSYS Fluent as the computational fluid dynamics (CFD) solver. The finite element solver under ANSYS Mechanical was employed for the structural problem, which solved the static elasticity force balance equations for a linearly elastic isotropic solid with geometrically nonlinear strains. The exchange of forces along the inner surface of the tube was performed by matching the full traction there as a boundary condition. A nonlinear iterative procedure transfers these loads incrementally until convergence is reached, ensuring a full two-way coupling. A typical simulation result of the displacement profile at steady state is shown in Fig. 4. Most importantly, this DNS approach *does not* make any of the assumptions the theory does, such as the lubrication approximation or those of a shell theory.

Next, we benchmark the flow rate–pressure drop relationship predicted by our mathematical theory. The results for Δp as a function of q are shown in Fig. 5 for (a) the specified Newtonian fluid and (b) the specified shear-thinning fluid. We see excellent agreement between theory and simulation, particularly for the smaller flow rates. At larger q , small but systematic differences emerge between theory and simulation because, at these flow rates, the deformation of the microtube starts to enter the non-linear strain regime, which is beyond the scope of the linear shell theory employed herein.

Having compared and verified the theoretical prediction for the hydrodynamics, namely the q – Δp relation, we now shift our focus to the solid domain. In Fig. 6, We plot the ratio of dimensionless radial tube deformation $\bar{u}_r(\bar{z})$ to the dimensionless pressure $\bar{p}(\bar{z})$ along the microtube’s length. Again, the results have been shown for both our chosen (a)

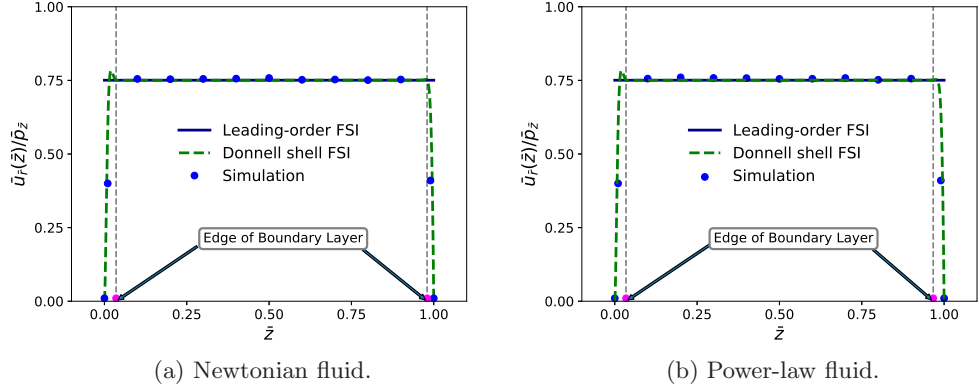


Figure 6: Ratio of the dimensionless radial deflection $\bar{u}_r(\bar{z})$ to the hydrodynamic pressure \bar{p} as a function of the axial position \bar{z} in the microtube. The leading-order FSI theory is given by Eq. (4.14), the Donnell shell FSI theory is the numerical solution of the TPBVP given by Eqs. (5.15) and (5.16) and the simulation results are from ANSYS. The edges of the clamping boundary layers, wherein end-effects tend to become important, are also highlighted.

Newtonian and (b) shear-thinning fluid. The leading-order perturbative result, namely Eq. (4.14), predicts this ratio to be $\bar{u}_r(\bar{z})/\bar{p}(\bar{z}) = (1 - \nu/2) = 3/4$ (a constant independent of \bar{z} !) for an incompressible material. For the beyond-leading-order analysis, we integrated Donnell's coupled equation, i.e., Eq. (5.14) describing the displacement once the pressure is eliminated, using the `solve_bvp` two-point BVP solver subroutine in Python's SciPy module (Jones *et al.* 2001). (We could have also plotted the matched asymptotic solution to Eq. (5.14), namely Eq. (5.40), but it would be indistinguishable for this value of $\epsilon = 6.25 \times 10^{-5}$ based on Table 1.) Figure 6 shows good agreement between the results of DNS and the two theories developed herein. Perhaps more interestingly, we observed that there is an extremely narrow region near the inlet ($\bar{z} = 0$) and outlet ($\bar{z} = 1$) planes, wherein the full ODE solution deviates significantly from the leading-order perturbative solution due to the presence of boundary layers as discussed in §5.3. The smallness of the boundary layer leads us to conclude that almost the entire tube, except a sliver near each end, is in a membrane state with negligible twisting and bending, as also discussed in (Dym 1990, Ch. 4).

6.4. Parameter space

The theory of linear FSI in microtubes for power-law fluids developed in this paper is hinges upon certain key assumptions. Thus, to complete our discussion, it is imperative to mention when the approximations used in our theory are valid, i.e., for what choices of the physical and geometric parameters does our theory accurately capture FSIs in microtubes. For example, even at vanishing Reynolds number microtube FSI can lead to buckling of the elastic structure and collapse of the flow passage (Heil 1997), which is beyond the applicability of our approach.

Thus, out for our linear FSI theory to hold true, we must require that

(i) $t/a \ll 1$: This inequality allows us to use the thin shell theory. A displacement solution can then be easily obtained perturbatively at the leading order in t/a , or via matched asymptotics to capture clamping boundary layers.

(ii) $U_c/a \ll 1$: The ratio of radial deflection to the radius should be small for the small-strain assumption of shell theory to be valid.

(iii) $a/\ell \ll 1$: This assumption allows us to simplify both the fluid mechanics and the structural mechanics problem under the assumption of a slender geometry. This assumption ensures, physically, the rotation of a shell element is negligible. This assumption also allows us to employ lubrication theory for the flow problem.

A natural ordering of the physical dimensions of the tubes thus follows:

$$U_c \ll t \ll a \ll \ell \quad (6.1)$$

must hold for the present linear FSI theory to apply.

7. Conclusions and outlook

In this paper, we have developed a theory of the fluid–structure interaction (FSI) between a generalized Newtonian fluid and a deformable circular cylinder at microscale. Specifically, we have formulated an expression relating the pressure drop and the flow rate taking into account both shear dependent viscosity and the softness of walls. Hinged on the assumptions pertaining to the geometry, the lubrication approximation has been employed to yield a unidirectional flow field. Similarly, the structural domain has been analyzed using three different linear shell theories, namely membrane theory, Donnell/Sanders shell theory. Coupling between the flow field and the structural domain was achieved both analytically, in a perturbative sense, and numerically using the “full” fifth-order ODE. Interestingly, all the structural models considered yield, at the leading-order in slenderness, exactly the same result, i.e., a linear relationship between the local radial deformation and the local hydrodynamic pressure. We also showed that the perturbative solution matches closely with the full-ODE solution obtained numerically by solving a nonlinear two-point BVP. The theoretical results were compared with two-way-coupled 3D simulations carried out using the commercial engineering software by ANSYS Inc. (2018). Acceptable levels of agreement were obtained in the parameter space, validating our FSI theory for non-Newtonian flow in deformable microtubes. Specifically, an important and counterintuitive result stemming from this work is that, due to the complex interplay between FSI and rheology, certain shear-*thickening* fluids flow more easily (i.e., require lower Δp to maintain a constant q) than certain shear-*thinning* fluids. This effect is observed for weak FSI (i.e., small β). Such an anomalous enhancement should be interrogated experimentally because it might be of use in lab-on-a-chip technologies.

In future work, the FSI theory developed here can be extended to incorporate further physical phenomena that arise in microscale fluid mechanics. For example, the material composing the tube may not be only elastic but also porous (i.e., *poroelastic*) (Auton & MacMinn 2017). Another direction is to consider microflows of gases in elastic tubes, which necessitates accounting for compressibility of the fluid (Elbaz *et al.* 2018) and possible wall slip (San & Staples 2012).

7.1. Comparison to viscous FSI in a rectangular channel: Plates vs. shells

As mentioned previously, the behavior of any slice of the soft microtube considered herein, as described by the leading-order deformation–pressure balance in Eq. (4.14) is akin to a Hookean spring, and it is independent of behavior of the neighboring slices. The latter aspect of the slender microtube is akin to that of slender microchannel with a soft top wall (Christov *et al.* 2018; Shidhore & Christov 2018; Anand *et al.* 2018), wherein each cross-sectional slice in the axial (flow-wise) direction decouples from neighboring

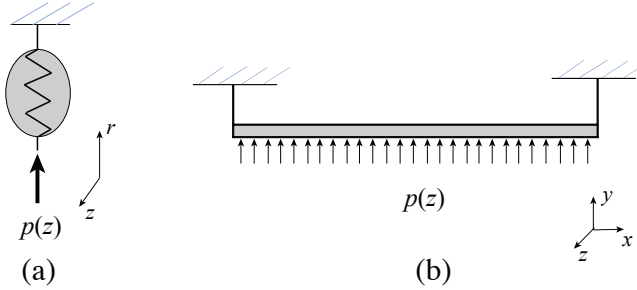


Figure 7: (a) A slice of a soft microtube represented as a Hookean spring. (b) A slice of a microchannel's soft top wall represented as an Euler beam. Both are uniformly loaded but the hydrodynamic pressure p at flow-wise cross-section z .

slices. However, the two cases should also be contrasted: for a long and shallow microchannel, each slice of the top wall acts like an Euler beam in the cross-sectional direction; meanwhile, for a slender microtube, each slice acts as a Hookean spring. This discussion is illustrated schematically in Fig. 7.

The Hookean spring analogy of elastic behavior of the microtube, as suggested by Eq. (4.14), means that each slice of microtube is more compliant and thus deforms more than a corresponding slice of a microchannel, which behaves like an Euler beam, with all other conditions being the same. This result is connected to the intuitive fact that only the microchannel's top wall is deformable, while the full circumference of the microtube is deformable.

We thank T. C. Shidhore for assistance with the initial forays into two-way ANSYS FSI simulations of microtubes and advice related to the latter. This research was, in part, supported by the US National Science Foundation under grant No. CBET-1705637.

Appendix A. Grid-independence study

To ensure that the converged solution which we obtain is independent of mesh size, we performed a grid independence study. Two grids each were defined for CFD and finite elements solver respectively, thus bringing the total number of grid arrangements to four. The details of the grids are shown in Table 2. For the CFD mesh, grid 2 was generated by scaling the number of edge divisions across the model in grid 1 by a factor of 2. Similarly, grid 2 for the FEM mesh was generated by increasing the number of divisions on the lateral surfaces from 500 to 800. Apart from the grid refinement, there was no further change in the model and the remaining properties were same as those mentioned in Table 1. For the grid refinement study, the simulations were carried out only for a single flow rate namely, 1 mL/min.

The results of the grid convergence study are shown in Fig. 8: Fig. 8(a) shows the average deflection over the circumference at the centerline of the tube, and Fig. 8(b) shows the pressure drop over the length of the microtube. These plots demonstrate that our simulation results are grid-independent.

Appendix B. Interplay between β and n and its effect on the pressure

The FSI parameter β and the power-law index n tend to have an opposite effect to each other on the pressure drop across the microtube, as highlighted in §6.1. While β

	CFD grid 1	CFD grid 2	FEM grid 1	FEM grid 2
Number of nodes	1,348,768	10,626,967	1,090,584	1,743,984
Number of elements	1,387,365	10,467,576	198,000	316,800

Table 2: The four grids used for the grid-convergence (mesh-independence) study.

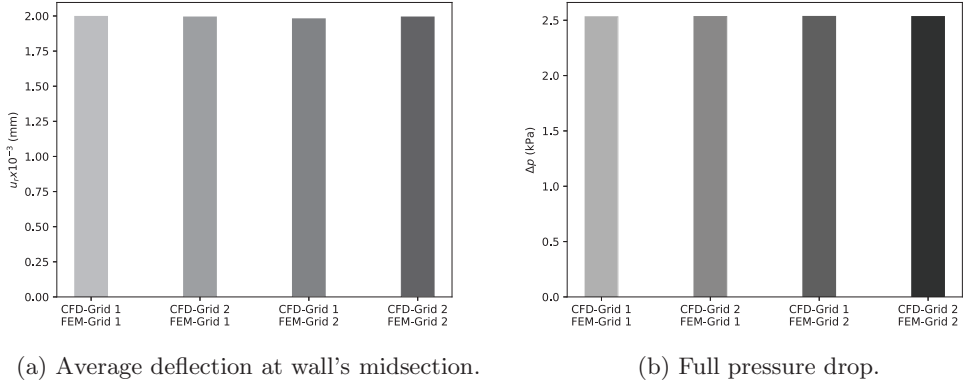


Figure 8: Grid-convergence (mesh-independence) study of the microtube simulations.

tends to reduce the pressure drop by allowing the flow to pass through a larger area, an increase in n leads to higher pressure drops via increased resistance to flow. Which of these effects dominates depends on the values of β and n . To understand this point, we differentiate Eq. (5.7) at $\bar{z} = 0$ with respect to n to obtain:

$$\frac{\partial \Delta \bar{p}}{\partial n} = \frac{1}{\beta(2+3n)^2} \left(\left[1 + 2(3+1/n)^n (2+3n) \beta \bar{q}^n \right]^{1/(2+3n)} 2\beta(3+1/n)^n (2+3n) \bar{q}^n \right. \\ \times \left\{ \frac{[1+6n+(2+9n(1+n))\ln(3+1/n)+(2+9n(1+n))\ln\bar{q}]}{1+3n+2\beta(3+1/n)^n(2+9n(1+n))\bar{q}^n} \right\} \\ \left. - 3 \ln [1 + 2\beta(3+1/n)^n (2+3n) \bar{q}^n] \right). \quad (B1)$$

The expression in Eq. (B1) is plotted as a function of β and n in Fig. 9 for (a) $\bar{q} = 1$ and (b) $\bar{q} = 3$. We observed that $\partial \Delta \bar{p} / \partial n$ is negative, except from small β (little FSI). Figure 9 further confirms our earlier observation (from §6.1) that for $\beta \ll 1$, $\Delta \bar{p}$ increases with n , but this trend is reversed for larger β , for which $\Delta \bar{p}$ decreases with n .

REFERENCES

ABGRALL, P. & GUÉ, A. M. 2007 Lab-on-chip technologies: Making a microfluidic network and coupling it into a complete microsystem - A review. *J. Micromech. Microeng.* **17**, R15.

ANAND, V., DAVID JR, J. & CHRISTOV, I. C. 2018 Non-Newtonian fluid-structure interactions: Static response of a microchannel due to internal flow of a power-law fluid. *preprint* (arXiv:1809.09065).

ANSYS INC. 2018 ANSYS® Academic Research Mechanical, Release 19.0 Help System, Coupled Field Analysis Guide, ANSYS, Inc. *Tech. Rep.*

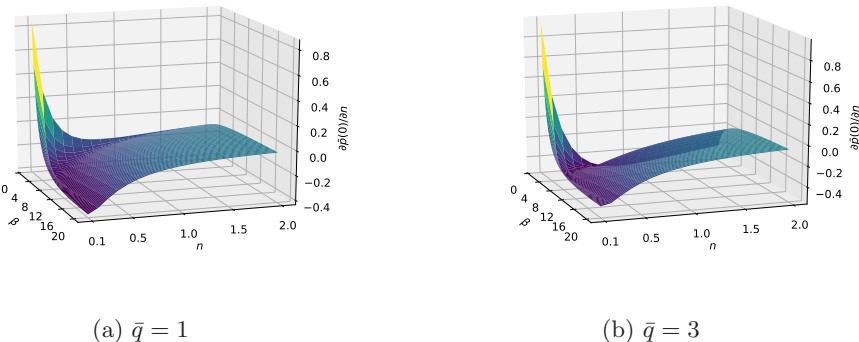


Figure 9: $\partial\Delta\bar{p}/\partial n$ as a function of β and n for (a) $\bar{q} = 1$ and (b) $\bar{q} = 3$. Both plots show that $\partial\Delta\bar{p}/\partial n$ is negative, except for small β .

AUROUX, P.-A., IOSSIFIDIS, D., REYES, D. R. & MANZ, A. 2002 Micro total analysis systems. 2. Analytical standard operations and applications. *Anal. Chem.* **74**, 2637–2652.

AUTON, L. C. & MACMINN, C. W. 2017 From arteries to boreholes: steady-state response of a poroelastic cylinder to fluid injection. *Proc. R. Soc. A* **473**, 20160753.

AYYASWAMY, P. S. 2016 Introduction to Biofluid Mechanics. In *Fluid Mechanics*, 6th edn. (ed. P. K. Kundu, I. M. Cohen & D. R. Dowling), chap. 16, pp. e1–e73. San Diego, CA: Academic Press, an imprint of Elsevier Inc.

BALMFORTH, N. J., FRIGAARD, I. A. & OVARLEZ, G. 2014 Yielding to stress: Recent developments in viscoplastic fluid mechanics. *Annu. Rev. Fluid Mech.* **46**, 121–146.

BAZILEVS, Y., TAKIZAWA, K. & TEZDUYAR, T. E. 2013 *Computational Fluid-Structure Interaction Methods and Applications*. Chichester, UK: John Wiley & Sons Inc.

BERTRAM, C. D. & PEDLEY, T. J. 1982 A mathematical model of unsteady collapsible tube behaviour. *J. Biomech.* **15**, 39–50.

BIRD, R. B. 1976 Useful non-Newtonian models. *Annu. Rev. Fluid Mech.* **8**, 13–34.

BIRD, R. B., ARMSTRONG, R. C. & HASSAGER, O. 1987 *Dynamics of Polymeric Liquids*, 2nd edn., , vol. 1. New York: John Wiley.

BOYKO, E., BERCOVICI, M. & GAT, A. D. 2017 Viscous-elastic dynamics of power-law fluids within an elastic cylinder. *Phys. Rev. Fluids* **2**, 073301.

BRUUS, H. 2008 *Theoretical Microfluidics*. Oxford, UK: Oxford University Press.

ĆANIĆ, S. & MIKELIĆ, A. 2003 Effective equations modeling the flow of a viscous incompressible fluid through a long elastic tube arising in the study of blood flow through small arteries. *SIAM J. Appl. Dyn. Syst.* **2**, 431–463.

CHAKRABORTY, D., PRAKASH, J. R., FRIEND, J. & YEO, L. 2012 Fluid-structure interaction in deformable microchannels. *Phys. Fluids* **24**, 102002.

CHAKRABORTY, S. 2005 Dynamics of capillary flow of blood into a microfluidic channel. *Lab Chip* **5**, 421–430.

CHIEN, S., USAMI, S., TAYLOR, H. M., LUNDBERG, J. L. & GREGERSEN, M. I. 1966 Effects of hematocrit and plasma proteins on human blood rheology at low shear rates. *J. Appl. Physiol.* **21**, 81–87.

CHOPIN, J., VELLA, D. & BOUDAOU, A. 2008 The liquid blister test. *Proc. R. Soc. A* **464**, 2887–2906.

CHRISTOV, I. C., COGNET, V., SHIDHORE, T. C. & STONE, H. A. 2018 Flow rate–pressure drop relation for deformable shallow microfluidic channels. *J. Fluid Mech.* **814**, 267–286.

CRESPI-LLORENS, D., VICENTE, P. & VIEDMA, A. 2015 Generalized Reynolds number and viscosity definitions for non-Newtonian fluid flow in ducts of non-uniform cross-section. *Exp. Thermal Fluid Sci.* **64**, 125–133.

DAVIS, S. H. 2017 The importance of being thin. *J. Eng. Math.* **105**, 3–30.

DIXIT, T. & GHOSH, I. 2015 Review of micro- and mini-channel heat sinks and heat exchangers for single phase fluids. *Renew. Sust. Energ. Rev.* **41**, 1298–1311.

DONNELL, L. H. 1933 Stability of thin-walled tubes under torsion. *Tech. Rep.* NACA-TR-479.

DUPRAT, C. & STONE, H. A., ed. 2016 *Fluid–Structure Interactions in Low-Reynolds-Number Flows*. Cambridge, UK: The Royal Society of Chemistry.

DYM, C. L. 1990 *Introduction to the Theory of Shells*. New York, NY: Hemisphere Publishing Corporation.

EBRAHIMI, A. P. 2009 Mechanical properties of normal and diseased cerebrovascular system. *J. Vasc. Interv. Neurol.* **2**, 155–162.

ELBAZ, S. B. & GAT, A. D. 2014 Dynamics of viscous liquid within a closed elastic cylinder subject to external forces with application to soft robotics. *J. Fluid Mech.* **758**, 221–237.

ELBAZ, S. B. & GAT, A. D. 2016 Axial creeping flow in the gap between a rigid cylinder and a concentric elastic tube. *J. Fluid Mech.* **806**, 580–602.

ELBAZ, S. B., JACOB, H. & GAT, A. D. 2018 Transient gas flow in elastic microchannels. *J. Fluid Mech.* **846**, 460–481.

FLÜGGE, W. 1960 *Stresses in Shells*. Berlin/Heidelberg: Springer.

FUNG, Y. C. 1993 *Biomechanics: Mechanical Properties of Living Tissues*. New York, NY: Springer-Verlag.

FUNG, Y. C. 1997 *Biomechanics: Circulation*, 2nd edn. New York, NY: Springer-Verlag.

GAY-BALMAZ, F., GEORGIEVSKII, D. & PUTKARADZE, V. 2018 Stability of helical tubes conveying fluid. *J. Fluids Struct.* **78**, 146–174.

GERVAIS, T., EL-ALI, J., GÜNTHER, A. & JENSEN, K. F. 2006 Flow-induced deformation of shallow microfluidic channels. *Lab Chip* **6**, 500–507.

GOMEZ, M., MOULTON, D. E. & VELLA, D. 2017 Passive control of viscous flow via elastic snap-through. *Phys. Rev. Lett.* **119**, 144502.

GROTBORG, J. B. 1994 Pulmonary flow and transport phenomena. *Annu. Rev. Fluid Mech.* **26**, 529–571.

GROTBORG, J. B. & JENSEN, O. E. 2004 Biofluid mechanics in flexible tubes. *Annu. Rev. Fluid Mech.* **36**, 121–147.

HAPPEL, J. R. & BRENNER, H. 1983 *Low Reynolds Number Hydrodynamics*, 2nd edn. The Hague: Martinus Nijhoff Publishers.

HARDY, B. S., UECHI, K., ZHEN, J. & KAVEHPOUR, H. P. 2009 The deformation of flexible PDMS microchannels under a pressure driven flow. *Lab Chip* **9**, 935–938.

HEIL, M. 1997 Stokes flow in collapsible tubes: computation and experiment. *J. Fluid Mech.* **353**, 285–312.

HEIL, M. & HAZEL, A. L. 2011 Fluid-structure interaction in internal physiological flows. *Annu. Rev. Fluid Mech.* **43**, 141–162.

HEWITT, I. J., BALMFORTH, N. J. & DE BRUYN, J. R. 2015 Elastic-plated gravity currents. *Eur. J. Appl. Math.* **26**, 1–31.

HOLMES, D. P., TAVAKOL, B., FROEHLICHER, G. & STONE, H. A. 2013 Control and manipulation of microfluidic flow via elastic deformations. *Soft Matter* **9**, 7049–7053.

HOLMES, M. H. 2013 *Introduction to Perturbation Methods, Texts in Applied Mathematics*, vol. 20. New York, NY: Springer Science+Business Media.

HUSSAIN, M. A., KAR, S. & PUNIYANI, R. R. 1999 Relationship between power law coefficients and major blood constituents affecting the whole blood viscosity. *J. Biosci.* **24**, 329–337.

JONES, E., OLIPHANT, T., PETERSON, P. & OTHERS 2001 SciPy: Open source scientific tools for Python. GitHub.

JUEL, A., PIHLER-PUZOVIĆ, D. & HEIL, M. 2018 Instabilities in blistering. *Annu. Rev. Fluid Mech.* **50**, 691–714.

KANG, C. K., ROH, C. H. & OVERFELT, R. A. 2014 Pressure-driven deformation with soft polydimethylsiloxane (PDMS) by a regular syringe pump: challenge to the classical fluid dynamics by comparison of experimental and theoretical results. *RSC Adv.* **4**, 3102–3112.

KARAN, P., CHAKRABORTY, J. & CHAKRABORTY, S. 2018 Small-scale flow with deformable boundaries. *J. Indian Inst. Sci.* **98**, 159–183.

KELLER, H. B. 1976 *Numerical Solution of Two Point Boundary Value Problems, CBMS-NSF Regional Conference Series in Applied Mathematics*, vol. 24. Philadelphia, PA: SIAM.

KITSON, P. J., ROSNES, M. H., SANS, V., DRAGONE, V. & CRONIN, L. 2012 Configurable 3D-Printed millifluidic and microfluidic 'lab on a chip' reactionware devices. *Lab Chip* **12**, 3267–3271.

KIZILOVA, N., HAMADICHE, M. & GAD-EL HAK, M. 2012 Mathematical models of biofluid flows in compliant ducts. *Arch. Mech.* **64**, 65–94.

KLEINSTREUER, C. 2006 *Biofluid Dynamics: Principles and Selected Applications*. Boca Raton, FL: CRC Press, an imprint of Taylor & Francis Group.

KONG, L. X., PEREBIKOVSKY, A., MOEBIUS, J., KULINSKY, L. & MADOU, M. 2016 Lab-on-a-CD. *J. Lab. Automat.* **21**, 323–355.

KRAUS, H. 1967 *Thin Elastic Shells*. New York, NY: John Wiley & Sons.

LAUGA, E. 2016 Bacterial hydrodynamics. *Annu. Rev. Fluid Mech.* **48**, 105–130.

LEAL, L. G. 2007 *Advanced Transport Phenomena: Fluid Mechanics and Convective Transport Processes*. New York, NY: Cambridge University Press.

LEE, L. J. 2006 BioMEMS. In *Encyclopedia of Chemical Processing* (ed. S. Lee), , vol. 1, pp. 161–169. New York: Taylor & Francis.

LESLIE, D. C., EASLEY, C. J., SEKER, E., KARLINSEY, J. M., UTZ, M., BEGLEY, M. R. & LANDERS, J. P. 2009 Frequency-specific flow control in microfluidic circuits with passive elastomeric features. *Nat. Phys.* **5**, 231–235.

LOVE, A. E. H. 1944 *A treatise on mathematical theory of elasticity*, 4th edn. New York: Dover Publications.

MADOU, M., ZOVAL, J., JIA, G., KIDO, H., KIM, J. & KIM, N. 2006 Lab on a CD. *Annu. Rev. Biomed. Eng.* **8**, 601–628.

MATSUMOTO, T., SUGITA, S. & YAGUCHI, T. 2015 Biomechanics of blood vessels: Structure, mechanics, and adaptation. In *Advances in Metallic Biomaterials, Springer Series in Biomaterials Science and Engineering*, vol. 3, chap. 4, pp. 71–98. Berlin/Heidelberg: Springer-Verlag.

MINDLIN, R. D. 1951 Influence of rotatory inertia and shear on flexural motions of isotropic, elastic plates. *ASME J. Appl. Mech.* **18**, 31–38.

NAGRATH, S., SEQUIST, L. V., MAHESWARAN, S., BELL, D. W., IRIMIA, D., ULKUS, L., SMITH, M. R., KWAK, E. L., DIGUMARTHY, S., MUZIKANSKY, A., RYAN, P., BALIS, U. J., TOMPKINS, R. G., HABER, D. A. & TONER, M. 2007 Isolation of rare circulating tumour cells in cancer patients by microchip technology. *Nature* **450**, 1235–1239.

NEU, J. C. 2015 *Singular Perturbation in the Physical Sciences, Graduate Studies in Mathematics*, vol. 167. Providence, RI: American Mathematical Society.

NGUYEN, N.-T. & WERELEY, S. T. 2006 *Fundamentals and Applications of Microfluidics*, 2nd edn. Norwood, MA: Artech House.

OZSUN, O., YAKHOT, V. & EKINCI, K. L. 2013 Non-invasive measurement of the pressure distribution in a deformable micro-channel. *J. Fluid Mech.* **734**, R1.

PEDLEY, T. J. 1980 *The Fluid Mechanics of Large Blood Vessels*. Cambridge: Cambridge University Press.

RAJ, A. & SEN, A. K. 2016 Flow-induced deformation of compliant microchannels and its effect on pressure-flow characteristics. *Microfluid. Nanofluid.* **20**, 31.

RAJ, M. K., DASGUPTA, S. & CHAKRABORTY, S. 2017 Hydrodynamics in deformable microchannels. *Microfluid. Nanofluid.* **21**, 70.

RAJ, M. K., CHAKRABORTY, J., DASGUPTA, S. & CHAKRABORTY, S. 2018 Flow-induced deformation in a microchannel with a non-Newtonian fluid. *Biomicrofluidics* **12**, 034116.

REYES, D. R., IOSSIFIDIS, D., AUROUX, P.-A. & MANZ, A. 2002 Micro total analysis systems. 1. Introduction, theory, and technology. *Anal. Chem.* **74**, 2623–2636.

RUBINOW, S. I. & KELLER, J. B. 1972 Flow of a viscous fluid through an elastic tube with applications to blood flow. *J. Theor. Biol.* **34**, 299–313.

SAN, O. & STAPLES, A. E. 2012 Dynamics of pulsatile flows through elastic microtubes. *Int. J. Appl. Mech.* **4**, 1250006.

SANDBERG, L. B., GRAY, W. R. & FRANZBLAU, C., ed. 1977 *Elastin and Elastic Tissue, Advances in Experimental Medicine and Biology*, vol. 79. New York: Plenum Press.

SANDERS JR., J. L. 1959 An improved first-approximation theory for thin shells. *Tech. Rep. NASA TR R-24*.

SEKER, E., LESLIE, D. C., HAJ-HARIRI, H., LANDERS, J. P., UTZ, M. & BEGLEY, M. R.

2009 Nonlinear pressure-flow relationships for passive microfluidic valves. *Lab Chip* **9**, 2691–2697.

SHAPIRO, A. H. 1977 Steady flow in collapsible tubes. *ASME J. Biomech. Eng.* **99**, 126–147.

SHIDHORE, T. C. & CHRISTOV, I. C. 2018 Static response of deformable microchannels: a comparative modelling study. *J. Phys.: Condens. Matter* **30**, 054002.

SQUIRES, T. M. & QUAKE, S. R. 2005 Microfluidics: Fluid physics at the nanoliter scale. *Rev. Mod. Phys.* **77**, 977–1026.

SU, W., COOK, B. S., FANG, Y. & TENTZERIS, M. M. 2016 Fully inkjet-printed microfluidics: A solution to low-cost rapid three-dimensional microfluidics fabrication with numerous electrical and sensing applications. *Sci. Rep.* **6**, 1–12.

SUN, J., MASTERTMAN-SMITH, M. D., GRAHAM, N. A., JIAO, J., MOTTAHEDAH, J., LAKS, D. R., OHASHI, M., DEJESUS, J., KAMEI, K. I., LEE, K. B., WANG, H., YU, Z.T. F., LU, Y. T., HOU, S., LI, K., LIU, M., ZHANG, N., WANG, S., ANGENIEUX, B., PANOSYAN, E., SAMUELS, E. R., PARK, J., WILLIAMS, D., KONKANKIT, V., NATHANSON, D., VAN DAM, R. M., PHELPS, M. E., WU, H., LIAU, L. M., MISCHEL, P. S., LAZAREFF, J. A., KORNBLUM, H. I., YONG, W. H., GRAEBER, T. G. & TSENG, H. R. 2010 A microfluidic platform for systems pathology: Multiparameter single-cell signaling measurements of clinical brain tumor specimens. *Cancer Res.* **70**, 6128–6138.

SUTERA, S. P. & SKALAK, R. 1993 The history of Poiseuille's Law. *Annu. Rev. Fluid Mech.* **25**, 1–19.

TAVAKOL, B., FROEHLICHER, G., STONE, H. A. & HOLMES, D. P. 2017 Extended lubrication theory: Improved estimates of flow in channels with variable geometry. *Proc. R. Soc. A* **473**, 20170234.

TIMOSHENKO, S. & WOINOWSKY-KRIEGER, S. 1959 *Theory of Plates and Shells*, 2nd edn. New York: McGraw-Hill.

WAGNER, N. J. & BRADY, J. F. 2009 Shear thickening in colloidal dispersions. *Phys. Today* **62** (10), 27–32.

WEISBERG, A., BAU, H. H. & ZEMEL, J. N. 1992 Analysis of microchannels for integrated cooling. *Int. J. Heat Mass Transfer* **35**, 2465–2474.

WHITESIDES, G. M. 2006 The origins and the future of microfluidics. *Nature* **442**, 368–373.

WHITTAKER, R. J., HEIL, M., JENSEN, O. E. & WATERS, S. L. 2010 A rational derivation of a tube law from shell theory. *Q. J. Mech. Appl. Math.* **63**, 465–496.

XIA, Y. & WHITESIDES, G. M. 1998 Soft Lithography. *Annu. Rev. Mater. Sci.* **28**, 153–184.